

Seismicity and seismotectonics of the Albstadt Shear Zone in the northern Alpine foreland

Sarah Mader^{1,*}, Joachim R. R. Ritter¹, Klaus Reicherter² and the AlpArray Working Group³

5 ¹ Karlsruhe Institute of Technology, Geophysical Institute, Hertzstr. 16, 76187 Karlsruhe, Germany

² RWTH Aachen University, Institute of Neotectonics and Natural Hazards Group, Lochnerstr. 4 – 20, 52056 Aachen, Germany

³ <http://www.alparray.ethz.ch>

* corresponding author: sarah.mader@kit.edu

Abstract. The region around the town Albstadt, SW Germany, was struck by four damaging earthquakes with magnitudes greater than five during the last century. Those earthquakes occurred along the Albstadt Shear Zone (ASZ) which is characterized by more or less continuous microseismicity. As there are no visible surface ruptures, visible which may be connected to the fault zone, we study its characteristics ~~can only be studied~~ by its seismicity distribution and faulting pattern.

15 We use the earthquake data of the state earthquake service of Baden-Württemberg from 2011 to 2018 and complement it with additional phase picks beginning in 2016 at the AlpArray and StressTransfer seismic networks in the vicinity of the ASZ. This extended dataset is used to determine new minimum 1-D seismic v_p and v_s velocity models and corresponding station delay times for earthquake relocation. Fault plane solutions are determined for selected events and ~~the direction of the principal maximum horizontal~~ stress directions ~~is~~ are derived.

20 The minimum 1-D seismic velocity models have a simple and stable layering with increasing velocity with depth in the upper crust. The corresponding station delay times can be well explained by the lateral depth variation of the crystalline basement. The relocated events align about north-south with most of the seismic activity between the towns of Tübingen and Albstadt east of the 9° E meridian. The events can be separated into several subclusters which indicate a segmentation of the ASZ. The majority of the ~~2536~~ determined fault plane solutions features ~~a~~-NNE-SSW strike, but also NNW-SSE striking fault planes are observed. The main fault plane associated with the ASZ is dipping steeply and the rake indicates mainly sinistral strike-slip, but we also find minor components of normal and reverse faulting. The determined direction of the maximum horizontal stress of ~~140-1497~~ $^\circ$ is in good agreement with prior studies. Down to ca. 7-8 km depth S_{Hmax} is bigger than S_V , below S_V is the main stress component. This resultThe direction of S_{Hmax} indicates that the stress field in the area of the ASZ is mainly generated by the regional plate driving forces as well as the Alpine topography.

hat formatiert: Tiefgestellt

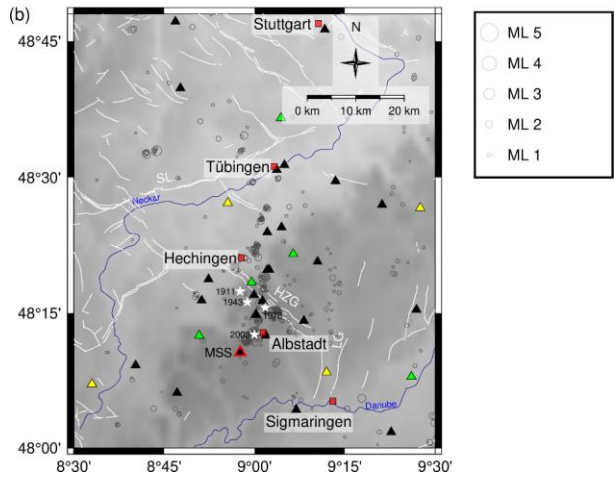
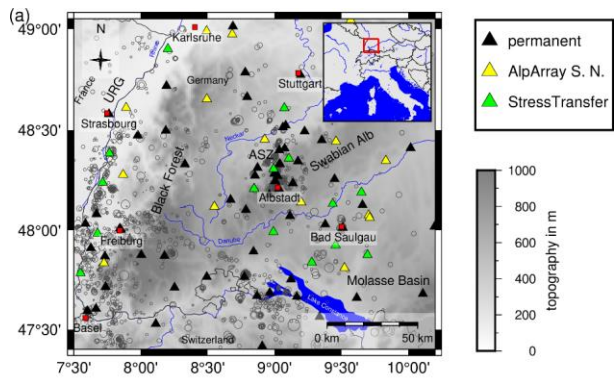
hat formatiert: Tiefgestellt

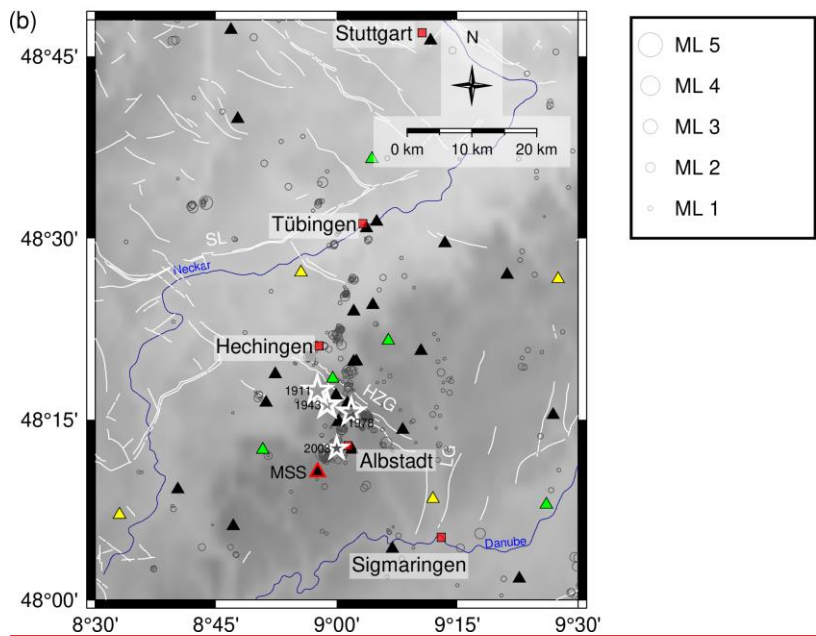
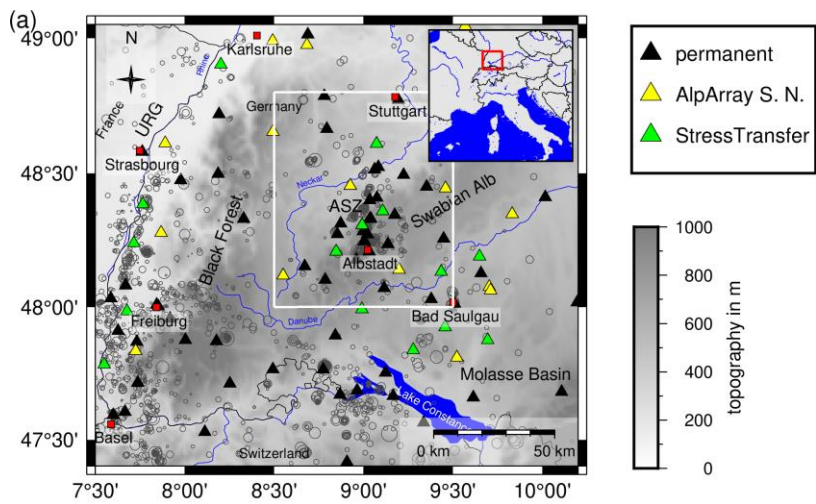
hat formatiert: Tiefgestellt

hat formatiert: Tiefgestellt

30 1 Introduction

The Swabian Alb near the town of Albstadt (Fig. 1) is one of the most seismically active regions in Central Europe (Grünthal and the GSHAP Region 3 Working Group, 1999). In the last century four earthquakes with magnitudes greater than 5 occurred in the region of the Albstadt Shear Zone (ASZ, Fig 1, e.g. Stange and Brüstle, 2005, Leydecker, 2011). Today such events could cause major damages with economic costs of several hundred





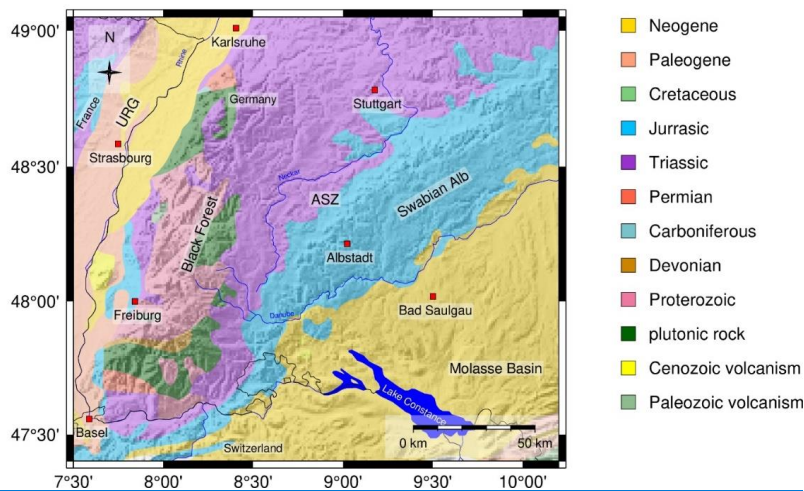


Fig. 1 a) Overview over our research area located in the southwest of Germany in the northern Alpine foreland. The ASZ is our research target (white framed area). Black triangles represent permanent seismic stations of the LED and other agencies. Yellow triangles represent temporary AlpArray seismic stations. Green triangles display the fifteen temporary seismic stations of the Stress Transfer network. The gray circles display the seismicity scaled by magnitude from 2011 to 2018. URG=Upper Rhine Graben

b) Close up of the area of the ASZ (white framed area in Fig. 1b). Symbols like in Fig. 1a. The red framed triangle highlights the central station Meßstetten (MSS) of the minimum 1-D seismic velocity model. White stars mark epicenters of the 4 strongest events with a magnitude greater than 5 in 1911, two in 1943 (same epicenter) and 1978, as well as the earthquake on 22nd March 2003 with a local magnitude of 4.4 (Leydecker, 2011), those events are not included in the earthquake catalog from 2011 to 2018 (gray circles scaled with magnitude like in Fig. 1a). White lines indicate known and assumed faults (Regierungspräsidium Freiburg, Landesamt für Geologie, Rohstoffe und Bergbau (Hrsg.), 2019). The Hohenzollern Graben (HZG) is the only clear morphological feature in the close vicinity to the ASZ. Other large tectonic features are the Lauchert Graben (LG) and the Swabian Line (SL).

Topography is based on the ETOPO1 Global Relief Model (Amante and Eakins, 2009).

c) Overview on the geology of the research area region, geology data is taken from Asch (2005).XXXXXXXXXX

Formatiert: Standard

million Euros (Tyagunov et al., 2006). Although the earthquakes caused major damage to buildings such as fractures in walls and damaged roofs or chimneys, no surface ruptures have been found or described (e.g. Schneider, 1971). For this reason, the ASZ can only be analyzed by its seismicity to derive its geometry, possible segmentation, and faulting pattern. One of the best observed earthquakes happened on 22nd March 2003 and it was described as a sinistral strike-slip fault with a strike of 16° from north (Stange and Brüstle, 2005). This faulting mechanism -which- is similar to the observations from prior models of former major events (e.g. Schneider, 1973, Turnovsky, 1981, Kunze, 1982). Since 2005 the seismic station network of the state earthquake service of Baden-Württemberg (LED) was changed and extended (Stange, 2018) and in summer 2015 the installation of the temporary Alp Array Seismic Network (AASN) started (Hetényi et al., 2018). In 2018 we started our project

60 StressTransfer, in which we investigate areas of distinct seismicity in the northern Alpine foreland of Southwest Germany and
the related stress field (Mader and Ritter, in print). ~~For this study we installed additional~~The StressTransfer network consist of
15 seismic stations, equipped with instruments of the Karlsruhe BroadBand Array (KABBA), in our research area (Fig. 1a).
Here we present a compilation of different datasets to refine hypocentral parameters of the ASZ. For this we analyze the
earthquake catalog of the LED from 2011 to 2018 (Bulletin-Files des Landeserdbendienstes B-W, 2018) and complement it
65 with additional phase picks from recordings of AASN (AlpArray Seismic Network, 2015) and our own StressTransfer seismic
stations. We calculate a new ~~minimum~~-1-D seismic velocity model and relocate the events. For ~~some several~~ relocated events
we calculate fault plane solutions. This procedure gives us a new view of the geometry of the ~~fault pattern at depth of~~in the
ASZ based on its ~~permanent~~-microseismic activity. Furthermore, we use the fault plane solutions to derive the orientation of
the main~~ximum~~ horizontal stress ~~S₁~~~~maximum~~ components in the area of the ASZ and discuss ~~these~~ with known results.

70 2 Geological and Tectonic Setting

Southwest Germany is an area of low to moderate seismicity. The most active fault zones are the Upper Rhine Graben (URG)
and the area of the ASZ and the Hohenzollern Graben system (HZG, Fig. 1b). In the region of the URG the seismicity is
distributed over a large area. In comparison, in our research area the seismicity clusters in the close area around the ASZ and
the HZG.

75 The ASZ is named after the town of Albstadt situated on the Swabian Alb, a mountain range in South Germany (Fig. 1a).
South Germany consists of several tectono-stratigraphic units, a polymetamorphic basement with a Mesozoic cover tilted
towards southeast to east due to extension in the URG (Fig. 1ca), associated with updoming (Reicherter et al., 2008, Meschede
and Warr, 2019). The URG forms the western tectonic boundary, whereas the eastern boundary comprises the crystalline
basement of the Bohemian Massif. To the south the foreland basin of the Alps (Molasse Basin, Fig. 1ca) frames the area in a
80 triangular shape. The Molasse Basin covers the whole area south of the Swabian Alb up to the Alpine mountain chain. It is
filled with Neogene terrestrial, freshwater and shallow marine sediments (Fig. 1c, Meschede and Warr, 2019). The Swabian
Alb is bounded by the rivers Neckar in the north and Danube in the south (Fig. 1a). The sedimentary layers of the Swabian
Alb, which consist of Jurassic limestone, marl, silt and clay, dip downwards by 4° to the southeast and disappear below the
Molasse Basin (Fig. 1ca) and the Alpine Mountain Chain (Meschede and Warr, 2019). The sedimentary cover of the Swabian
85 Alb forms a typical cuesta landscape with major escarpments built up by resistant carbonates of the Late Jurassic that is cut by
several large fault systems, which are detectable in the present-day topography (Reicherter et al., 2008). The Black Forest to
the west of the Swabian Alb experienced the most extensive uplift due to the extension of the URG. Here, even metamorphic
and magmatic rocks of the Paleozoic basement are exposed. To the north and northwest of the Swabian Alb, Triassic rocks are
cropping out (Meschede and Warr, 2019). Due to the different uplift and erosional states of South Germany the depth of the
90 crystalline basement varies strongly between -5.4 km and 1.2 km above sea level (Rupf and Nitsch, 2008).

The current regional stress field of southwest Germany is dominated by an average horizontal stress orientation of 150° (e.g. Müller et al., 1992, Plenefisch and Bonjer (1997), Reinecker et al., 2010, Heidbach et al., 2016) and was determined from focal mechanism solutions, overcoring, borehole breakouts and hydraulic fracturing (e.g. Bonjer, 1997, Plenefisch & Bonjer, 1997, Kastrup et al., 2004, Reiter et al., 2015, Heidbach et al., 2016). It is characterized by NW-SE horizontal compression and NE-SW extension (e.g. Kastrup et al., 2004) and developed during late Miocene (Becker 1993). Analysis of several kinematic indicators hint that fault planes were already activated repeatedly during the Cenozoic (Reicherter et al., 2008). Three main groups of fault planes can be observed. First, NNE-SSW to N-S striking mainly sinistral fault planes, which are similar to the ASZ or the Lauchert Geraben (Fig. 1b) and parallel the URG. Second, NW-SE striking normal and/or dextral strike-slip fault planes, which correspond to the HZG in our area. Older kinematic indicators, like fibre tension gashes and stylolites, hint a sinistral initiation of those NW-SE striking fault planes during the Late Cretaceous-Paleogene with a maximum horizontal compression in NE-SW direction (Reicherter et al., 2008). And third, ENE-WSW oriented fault planes, which are mainly inactive, but some exhibit dextral strike-slip or reverse movement, for example the Swabian Line (Schwäbisches Lineament, Fig. 1b). The direction of S_{Hmax} stress field in our research area is quite constant, except of an area directly south of the HZG (Albstadt-Truchelfingen) and within the HZG (Albstadt-Onstmettingen). There the S_{Hmax} direction rotates about 20° counterclockwise into the strike of the HZG (130°, Baumann, 1986), which may be caused by a reduced marginal shear resistance.

The only morphologically visible tectonic feature close to Albstadt is the HZG (Fig. 1b), a small graben with an inversion of relief and a NW-SE strike (Schädel, 1976, Reinecker and Schneider, 2002). The 25 km long HZG has dip angles between 60-70° at the main faults and a maximum graben width of 1.5 km, which leads to a convergence depth of the main faults in 2-3 km depth (Schädel, 1976). Thus, the HZG is interpreted as a rather shallow tectonic feature. To the north and south of Albstadt there are further similar graben structures like the HZG, namely the Filder Geraben, Rottenburg Flexure, western Lake Constance faults, and Hegau which are also about parallel to the main horizontal stress field (Reinecker et al., 2010) like the HZG. Reinecker and Schneider (2002) propose a tectonic model to relate the graben structures with the ASZ below. They apply the result of Tron and Brun (1991), who showed that the movement of a partly decoupled strike-slip fault in the subsurface can generate graben structures at the surface in a steplike arrangement. In the regional tectonic model the graben structures are the HZG, the Rottenburg Flexure, western Lake Constance faults and the Filder Graben (Reinecker and Schneider, 2002). In their model, the graben structures are en-echelon features compensating the displacement of the ASZ. The ASZ itself is the strike-slip fault, partly decoupled from the surface by a layer of Middle Triassic evaporites of the salinar formation of the Middle Triassic from the overlying sedimentary layers (Reinecker and Schneider, 2002). Stange and Brüstle (2005) consider the bottom of the Mesozoic sediments as mechanical decoupling horizon as no earthquakes occur above 2 km depth.

Another tectonic feature in our research area is the ENE-WSW striking Swabian Line north of the river Neckar (Fig. 1b). It extends from the Black Forest area partly parallel along the cuesta of the Swabian Alb to the east (Reicherter et al., 2008, Fig.

hat formatiert: Schriftfarbe: Automatisch

125 ~~h~~). The sense of movement along the Swabian Line is dextral. To the east of the ASZ near Sigmaringen the Lauchert ~~G~~eraben strikes north-south, around parallel to the ASZ with a sinistral sense of displacement (Geyer and Gwinner, 2011, Fig. 1b).

The faults in southwest Germany exhibit mainly moderate displacements during the last ca. 5 Myr (Reicherter et al., 2008). At the HZG, for example, the maximum vertical offset is of the order of 100 ~~to~~ 150 m. The horizontal offset is considerably lower and more difficult to determine (Reicherter et al., 2008).

130 Along the 9°E meridian Wetzel and Franzke (2003) identified a 5-10 km broad zone of lineations pursuable from Stuttgart to Lake Constance (Fig. 1a). Those lineations strike predominantly N-S, NW-SW and ENE-WSW. The N-S and ENE-WSW striking faults limited the NW-SE striking graben structures, like the HZG (Reicherter et al., 2008). The NW-SE striking faults are expected to be possibly active at intersections with N-S striking faults due to a reduction in shear resistance accompanied by aseismic creep (Schneider, 1979, Schneider, 1993, Wetzel and Franzke, 2003).

135 ~~Wetzel and Franzke (2003) identified a 5 to 10 km broad zone along the 9° E meridian of lineations striking predominantly N-S, NW-SW and ENE-WSW pursuable from Stuttgart to Lake Constance. The graben structures, like the HZG, are limit by the NW-SE striking faults (Reicherter et al., 2008). Those faults are expected to be possibly active at intersections with N-S striking faults due to a reduction in shear resistance accompanied by aseismic creep (Schneider, 1979, Schneider, 1993, Wetzel and Franzke, 2003).~~

140 The first documented earthquakes in the area of the ASZ occurred in 1655 near Tübingen and had an intensity of 7 to 7.5 (Leydecker, 2011). A similarly strong earthquake occurred in 1911 near Albstadt-Ebingen with a local magnitude of 6.1 (Fig. 1b, Leydecker, 2011), causing damage to buildings (Reicherter et al., 2008). The seismic shock triggered landslides with surface scarps in both the superficial Quaternary deposits as well as the Tertiary Molasse sediments (Sieberg and Lais, 1925) in the epicentral area and close to Lake Constance, demonstrating the potential of hazardous secondary earthquake effects (Reicherter et al., 2008). Since the 1911 earthquake the Swabian Alb is one of the most seismically active regions in the

145 northern Alpine foreland with in total three more earthquakes with a local magnitude greater than 5 (Fig. 1b, ~~2x events in~~ 1943, 1978, e.g. Reinecker and Schneider, 2002, Stange and Brüstle, 2005). The latest strong events occurred on 4th November 2019 (ML 3.8) and 27th January 2020 (ML 3.5), with ML of 3.8 and 3.5 and 1 December 2020 (ML 4.4), Regierungspräsidium Freiburg, Landesamt für Geologie, Rohstoffe und Bergbau, 2020). The average seismic dislocation rates along the ASZ are on the order of 0.1 mm/a, respectively (Schneider, 1993). The return period of earthquakes along the ASZ with a magnitude of 5

150 is approximately 1000 years (Schneider, 1980, Reinecker and Schneider, 2002). Both estimates are based on historic earthquake records. From aftershock analyses and focal mechanism calculations we know that the ASZ is a steep NNE to SSW oriented sinistral strike-slip fault (e.g. Haessler et al., 1980, Turnovsky, 1981, Stange and Brüstle, 2005) in the crystalline basement, as all earthquakes occur in-at a depth greater than 2 km (Stange and Brüstle, 2005). The N-S-extension lateral extend of the fault zone in N-S direction is still under debate: Reinecker and Schneider (2002) propose an extension from Northern

155 Switzerland towards north to the area of Stuttgart, whereas Stange and Brüstle (2005) do not find this large extension as most of the seismicity happens on the Swabian Alb.

hat formatiert: Deutsch (Deutschland)

hat formatiert: Deutsch (Deutschland)

hat formatiert: Deutsch (Deutschland)

3 Earthquake Data & Station Network

As basis for our study we use the earthquake catalog of the LED from 2011 to 2018 for earthquakes within the area close to the ASZ (8.5-9.5° E, 48-48.8° N, Fig. 1b). For these 575 earthquakes we received the bulletin files of the LED (Bulletin-Files des Landeserdbendienstes B-W, 2018), consisting of hypocenter location, origin time, local magnitude M_L and all phase travel time picks with corresponding quality and P-phase polarity. The LED picks from 2011 to 2018 are from 51 LED seismic stations and 14 seismic stations run by other agencies like the state earthquake service of Switzerland (Fig. 1a). Locations are determined with HYPOPLUS, a Hypoinverse variant modified after Oncescu et al. (1996) which allows the usage of a 1.5-D seismic velocity model approach (Stange and Brüstle 2005). Most hypocenter depths are well determined, but around 9.7% of the depth values are manually fixed. The median uncertainty for longitude, latitude and depth within the catalog are: 0.5 km, 0.6 km, and 2.0 km, respectively. The magnitude M_L ranges from 0.0 to 3.4 with average uncertainties of about ± 0.2 and the magnitude of completeness is around $M_L 0.6$ (see Fig. S1XXX in the appendix). The used catalog only contains natural events, as quarry blasts are sorted out and induced events do not occur in the study region.

Additionally, within the AlpArray Project (Hetényi et al., 2018), nine seismic stations were installed ~~starting in~~ beginning in summer 2015 within 80 km distance to the ASZ, four of them directly around the ASZ (AlpArray Seismic Network, 2015, Fig. 1b). To get an even denser network and to detect microseismicity we started to install another 15 seismic broadband stations from the KABBA beginning in July 2018 in areas with striking seismicity in the northern Alpine foreland within our project StressTransfer (Fig. 1a) (Mader and Ritter, in print). Five of those stations are located in the vicinity of the ASZ (Fig. 1b) and three of them were already running at the end of 2018.

We complemented the LED catalog with additional seismic P- and S-phase picks from the four AASN stations located around the ASZ from 2016 to 2018 and our StressTransfer stations recording in 2018. In total, our combined dataset consists of 575 earthquakes (Fig. 1b) with 4521 direct P- and 4567 direct S-phase travel time picks from 69 seismic stations.

4 Data Processing

4.1 Phase Picking

To complement the LED catalog, we use a self-written code in ObsPy (e.g. Beyreuther et al., 2010) for semi-automatic manual picking of the direct P- and S-phases. The raw waveform recordings are bandpass filtered with a zero-phase four corners butterworth filter from 3 Hz to 15 Hz. Using the hypocenter coordinates of the LED we calculate an approximate arrival time at a seismic station. Around this arrival time, we define a noise and a signal time window following Diehl et al. (2012), so that we can calculate the signal to noise ratio (SNR) of our phase onsets. Our code calculates automatically the earliest possible pick (ep) and the latest possible pick (lp) (see Diehl et al., 2012) to get consistent error boundaries for each pick. Finally, the error boundaries are checked by eye, and the phase pick is done manually between the two error boundaries. The qualities of

hat formatiert: Nicht Hervorheben

hat formatiert: Nicht Hervorheben

0 up to 4 of the picked arrival time are set depending on the time difference between t_p and t_s (Table A1). For consistency a similar relationship is used between picking quality and uncertainty as defined by the LED (Bulletin-Files des Landeserdbebendienstes B-W, 2018).

4.2 Inversion for Minimum 1-D Seismic Velocity Models with VELEST

The LED uses the program HYPOPLUS (Oncescu et al., 1996) (Stange and Brüstle, 2005) for routine location, with which one can apply a 1.5-dimensional approach by using several 1-D seismic velocity models for selected regions (Stange and Brüstle, 2005, Bulletin-Files des Landeserdbebendienstes B-W, 2018). They use two P-wave velocity (v_p) models, a Swabian Jura model and a model for the state of Baden-Württemberg, and they define the S-wave velocity (v_s) model by a constant v_p/v_s -ratio (Stange and Brüstle, 2005, Bulletin-Files des Landeserdbebendienstes B-W, 2018, Fig. 4a) & b)). Furthermore, no station delay times are used (Bulletin-Files des Landeserdbebendienstes B-W, 2018).

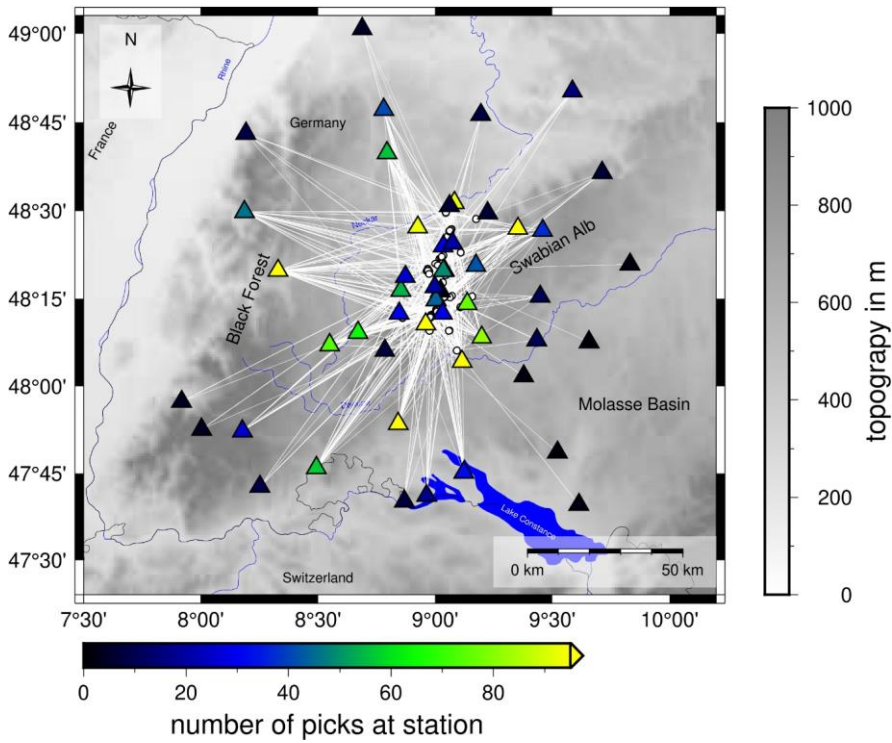
To determine a complemented catalog, we invert for new minimum 1-D seismic v_p and v_s models in the region of the ASZ with station delay times, using the program VELEST (Kissling et al., 1994, Kissling et al., 1995, VELEST Version 4.5). As central recording station we chose the station Meßstetten (MSS, Fig. 1b) as this station was running during our complete observational period and it is the oldest seismic recording site on the Swabian Alb, recording since 2nd June 1933 (Hiller, 1933). To get the best subset of our catalog for the inversion, we select only events with at least eight P-arrival times for the inversion for v_p and either eight P- or eight S- arrival times for the simultaneous inversion for v_p and v_s . The P-pick times exhibit a quality of 1 or better and the S-picks need a quality of 2 or better (Table A1). Events outside of the region of interest, 48.17 °N – 48.50 °N and 8.75 °E – 9.15 °E, with an azimuthal GAP greater than 150° and an epicentral distance of more than 80 km are rejected. This selection leads to a high-quality subset of 68 events with 789 P-phase picks for v_p and 99 events with 945 P-picks and 1019 S-phase picks for the v_p and v_s inversion (Fig. 2). We apply a staggered inversion scheme after Kissling et al. (1995) and Gräber (1993), first inverting for v_p and then for v_p and v_s together while damping the v_p model. The inversion for station delay times was done after the change in velocity was stable.

To probe our seismic velocity model space, inversions with 84 different starting models are calculated with 4 differently layered models from seismic refraction profile interpretations (Gajewski and Prodehl, 1985, Gajewski et al., 1987, Aichroth et al., 1992), the LED Swabian Jura model (Stange and Brüstle, 2005) and realistic random v_p variations (Fig. 3). We apply a staggered inversion scheme after Kissling et al. (1995) and Gräber (1993), first inverting for v_p and then for v_p and v_s together while damping the v_p model. The inversion for v_p was done with the 84 different starting models described before, always using the resulting velocity model of the prior inversion as input for the next inversion with VELEST. After 3 to 4 inversion runs the velocity models converged and the results did not change (Fig. 3). Then the inversion for station delay times was done. The minimum 1-D v_p model with the smallest RMS and the simplest layering was selected as final v_p model for the simultaneous v_p and v_s inversion. Together with a v_p/v_s -ratio of 1.69 (Stange and Brüstle, 2005) it was also used to calculate the v_s starting model, which was randomly changed to get in total 21 v_s starting models (Fig. 3), the inversion was done like

hat formatiert: Schriftart: Kursiv

220 the staggered inversion for v_p . The resulting minimum 1-D v_p and v_s models (ASZmod1, Fig. 4) were selected due to their small RMS.

hat formatiert: Schriftart: Kursiv



225 Fig. 2 Ray coverage and input data set for the inversion with VELEST. White circles represent the 99 selected events which are used for v_p and v_s inversion. Seismic stations are indicated as triangles and color-coded with the number of high quality picks at a station used for the v_p and v_s inversion. Topography is based on the ETOPO1 Global Relief Model (Amante and Eakins, 2009).

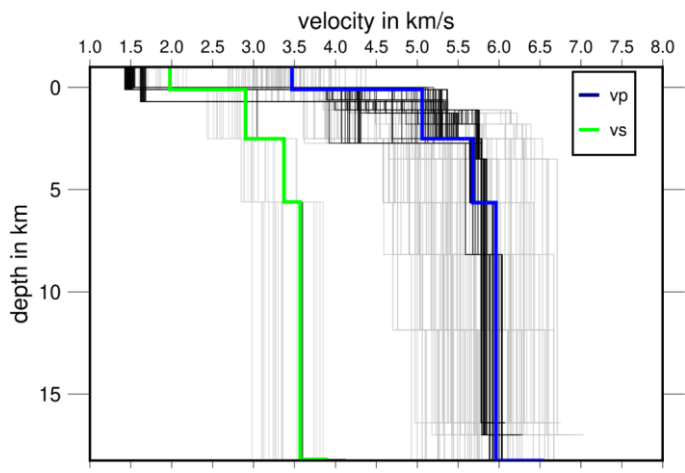


Fig. 3 VELEST input models for v_p (84) and v_s (21) (gray) and output v_p (84) and v_s (21) after inversion (black) together with the chosen model ASZmod1 (colored). A good convergence of the models can be observed, especially for v_s . The second layer converges worst. An instability of the first layer with a tendency to unrealistic low seismic velocities can be seen. For this reason, the velocity of ASZmod1 was fixed in the first layer.

To probe our seismic velocity model space, inversions with 84 different starting models are calculated with 4 differently layered models from seismic refraction profile interpretations (Gajewski and Prodehl, 1985, Gajewski et al., 1987, Aichroth et al., 1992), the LED Swabian Jura model (Stange and Brüstle, 2005) and realistic random v_p variations (Fig. 3). The minimum 1-D v_p model with the smallest RMS and the simplest layering was selected as final v_p model for the simultaneous v_p and v_s inversion. Together with a v_p/v_s ratio of 1.69 (Stange and Brüstle, 2005) it was also used to calculate the v_s starting model, which was randomly changed to get in total 21 v_s starting models (Fig. 3). The resulting minimum 1-D v_p and v_s models (ASZmod1, Fig. 4) were selected due to their small RMS.

To test the stability of ASZmod1 we randomly shifted all 99 events in space by maximum 0.1° horizontally and 5 km with depth (Kissling et al., 1995). The result of this shift test demonstrates that we can determine stable hypocenters, with an average deviation of less than 0.005° horizontally and of less than 2 km in depth for more than 90% of the events in the catalog (Fig. S12). The seismic velocities are stable except for the first and second layer (Fig. S32a and b). The first layer was unstable already during the inversion process (Fig. 3), therefore we damped its layer velocities and set them to realistic v_p and v_s values, based on the seismic v_p of the refraction profile interpretations (Gajewski et al., 1987). The instability in both upper layers may be caused by a few refracting rays and therefore small horizontal raylengths through the layers as well as only few

earthquakes within these layers (Fig. S32c). In total, the stability test (Fig. S24 and S32) indicates that the model represents the data and region very well and that the determined hypocenter locations are stable.

250

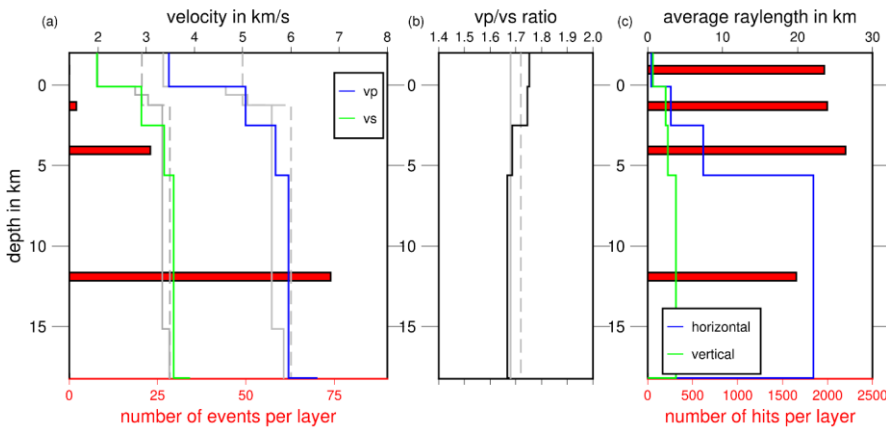


Fig. 4 a) Final minimum 1-D seismic velocity models (ASZmod1), v_s in green, v_p in blue. Gray lines represent velocity models of the LED (Bulletin-Files des Landeserdbendienstes B-W), solid: Swabian Jura models, dashed: Baden-Württemberg models. Red bars are scaled with the number of events in each layer of the velocity model.

255

b) v_p/v_s -ratio of ASZmod2 and the LED models.

c) Ray statistics of used ray paths. Red bars display number of hits per layer. Blue and green line give the average horizontal and vertical raylength.

260

We calculated an error estimate based on the variation of the 21 output v_p and v_s models with our chosen layer model of Gajewski et al. (1987) for ASZmod1 (Table 1). For a precise estimation we determined two times the standard deviation (2σ) of the velocity models for each layer. For the uppermost layer we could not estimate any error, as the first layer was manually set and strongly damped during the inversion process. The 2σ range is small for the third and fourth layers. This was expected as most of the events are located within those layers and as all other models, also with different layering, converge to similar velocities in those layers (Fig. 3). The error estimate for the second layer has to be considered carefully as this layer revealed strong instabilities during the stability test (Fig. S32). The fifth layer also has larger 2σ uncertainties relative to layers three and four, which is caused by less ray coverage and no events located below 18.25 km depth.

265

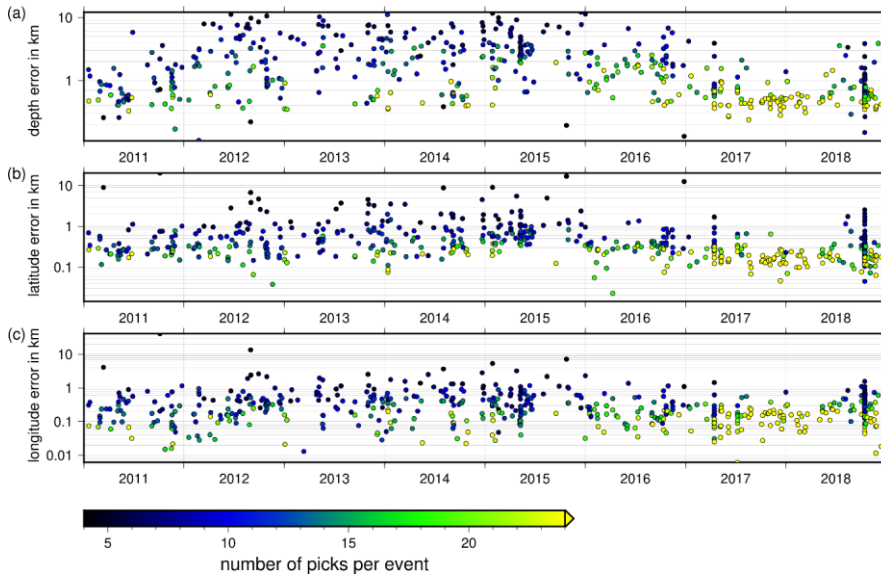
	Layer top in km	v_p in km/s	$2\sigma v_p$ in km/s	v_s in km/s	$2\sigma v_s$ in km/s
Layer 1	-2	3.47	-	1.98	-
Layer 2	0.1	5.06	0.30	2.90	0.06
Layer 3	2.5	5.68	0.03	3.37	0.01
Layer 4	5.63	5.95	0.02	3.57	0.01
Layer 5	18.25	6.55	0.31	3.91	0.32

Table 1 ASZmod1 with corresponding error estimates based on 2σ .

4.3 Relocation, Station Corrections and Error Estimation with NonLinLoc

270 To relocate the complete earthquake catalog we use the program NonLinLoc (NLL, Lomax et al., 2000), a non-linear oct-tree search algorithm. NLL calculates travel time tables after the eikonal finite-difference scheme of Podvin and Lecomte (1991) on a predefined grid, here with 1 km grid spacing. With the implemented oct-tree search algorithm (density) plots of the probability density function (pdf) of each event are determined after the inversion approach of Tarantola and Valette (1982) with either the L2-RMS likelihood function (L2) or the Equal Differential Time likelihood function (EDT). The determined pdf contains location uncertainties due to phase arrival time errors, theoretical travel time estimation errors, and the geometry of the network (Husen et al., 2003). Based on the pdfs an error ellipsoid (68% confidence) is determined, which we use to calculate latitude, longitude, and depth error estimates for each earthquake (Fig. 5). The estimated errors of our events are getting smaller beginning in 2016, especially the depth error estimate. This reduction correlates well with the increased number of picks per event, so with the increased number of seismic stations around the ASZ due to the modification of the LED network and the installation of the AASN and the StressTransfer stations [from 2018](#) (Hetényi et al., 2018, Stange, 2018, Fig. 5). As final hypocenter solution the maximum likelihood hypocenter is selected, which corresponds to the minimum of the pdf.

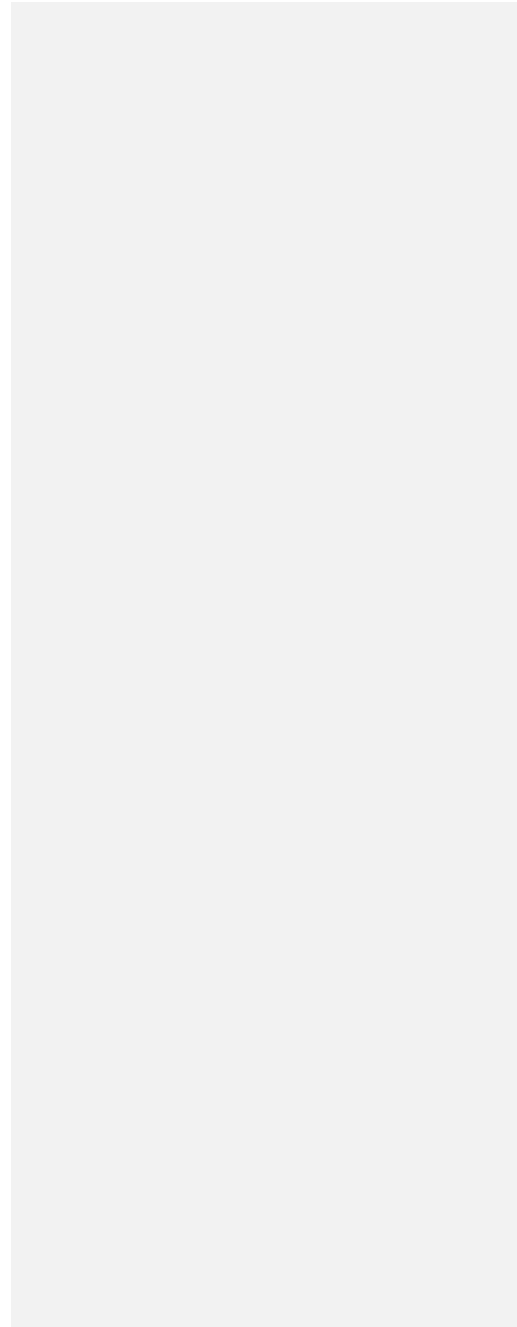
285 We compared the resulting hypocenters and error estimates using the L2 or the EDT likelihood function. The comparison mainly indicates similar earthquake locations, but we find EDT errors (Fig. S34) for many events which are too large and also unrealistic (some greater than 50 km, leading to hypocenter shifts across the whole region). For this reason, we decided to use L2 for relocating our combined catalog.

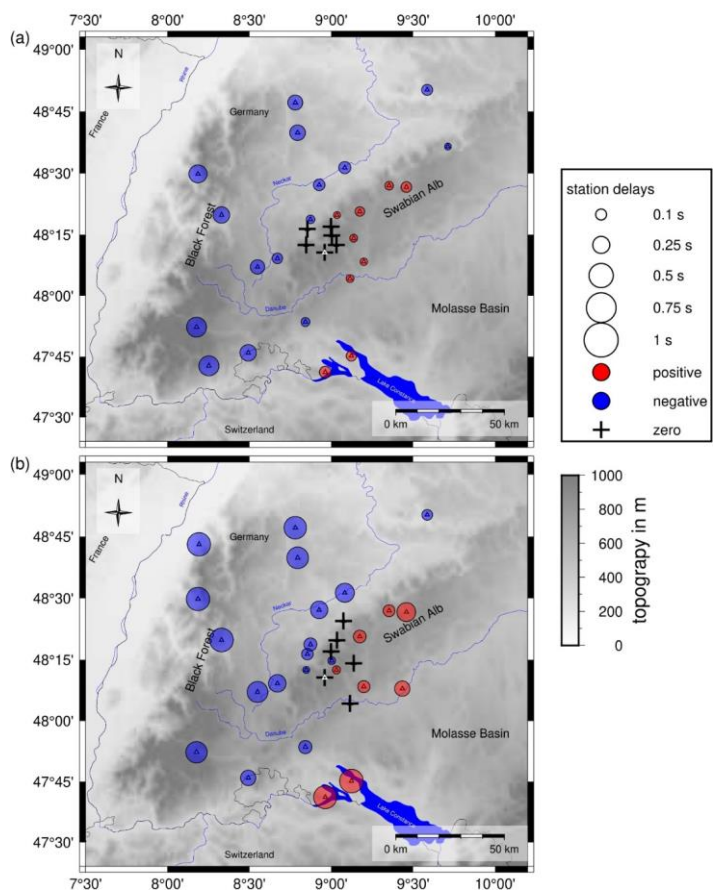


290 **Fig. 5** Errors calculated from the 68% confidence ellipsoid from NLL with L2 (L2-RMS likelihood function) for each event in the combined catalog for (a) depth, (b) latitude, and (c) longitude. The errors are color-coded depending on the number of picks, with dark colors indicating less picks and bright colors many picks. Hypocenters with many observations are determined with smaller errors in depth and lateral position.

In NNL one can examine station delay times calculated from the station residuals. The station delay times are defined as the time correction subtracted from the observed P- and S- wave arrival times. This implies that negative station delay times exhibit faster velocities relative to ASZmod1 and positive station delay times exhibit slower velocities relative to ASZmod1. We used ASZmod1 and the corresponding VELEST station delay times as well as our high-quality subset of 99 earthquakes as input for NLL. After four iterative runs of NLL, with always using the output station delay times as new input station delay times, the determined station delay times become stable. As we want to relocate the whole catalog with NLL, we use for consistency the with NLL updated VELEST station delay times. Since ASZmod1 is a 1-D seismic velocity model below the reference station MSS, we expect the station delay times to become zero for MSS. After four iterative runs the actually determined station delay times of MSS are 0.014 s with σ of 0.083 s for v_p and -0.027 s with σ of 0.064 s for v_s . As σ is bigger than the actual station delay time and the station delay time of MSS is smaller than the maximum error range of 0.05 s of our best

300





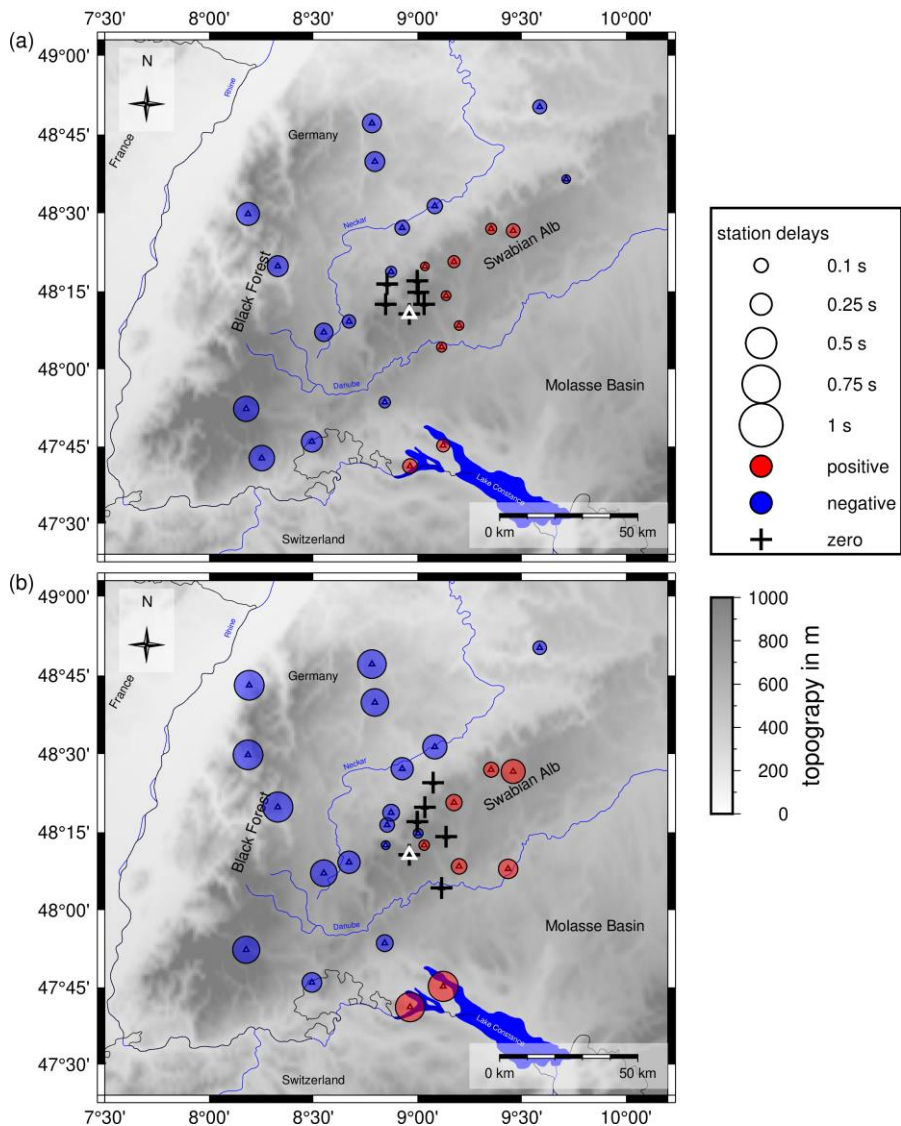


Fig 6 a) station delay times for the v_p velocity model ASZmod1

b) station delay times for the v_s velocity model ASZmod1

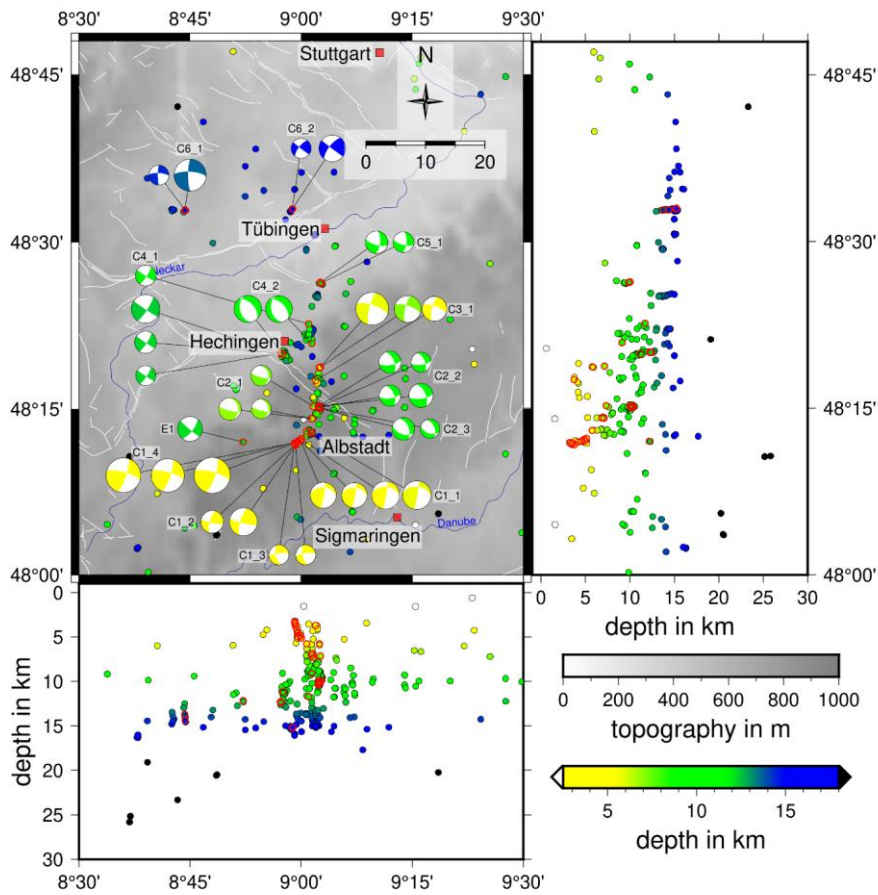
310 **Blue colored circles represent negative station delay times, indicating areas with faster velocities than ASZmod1. Red colored circles illustrate positive station delay times, indicating slower velocities than ASZmod1. Crosses are stations with zero station delays. Only stations with more than 5 travel time picks are included. Small white triangle highlights reference station MSS. Topography is based on the ETOPO1 Global Relief Model (Amante and Eakins, 2009).**

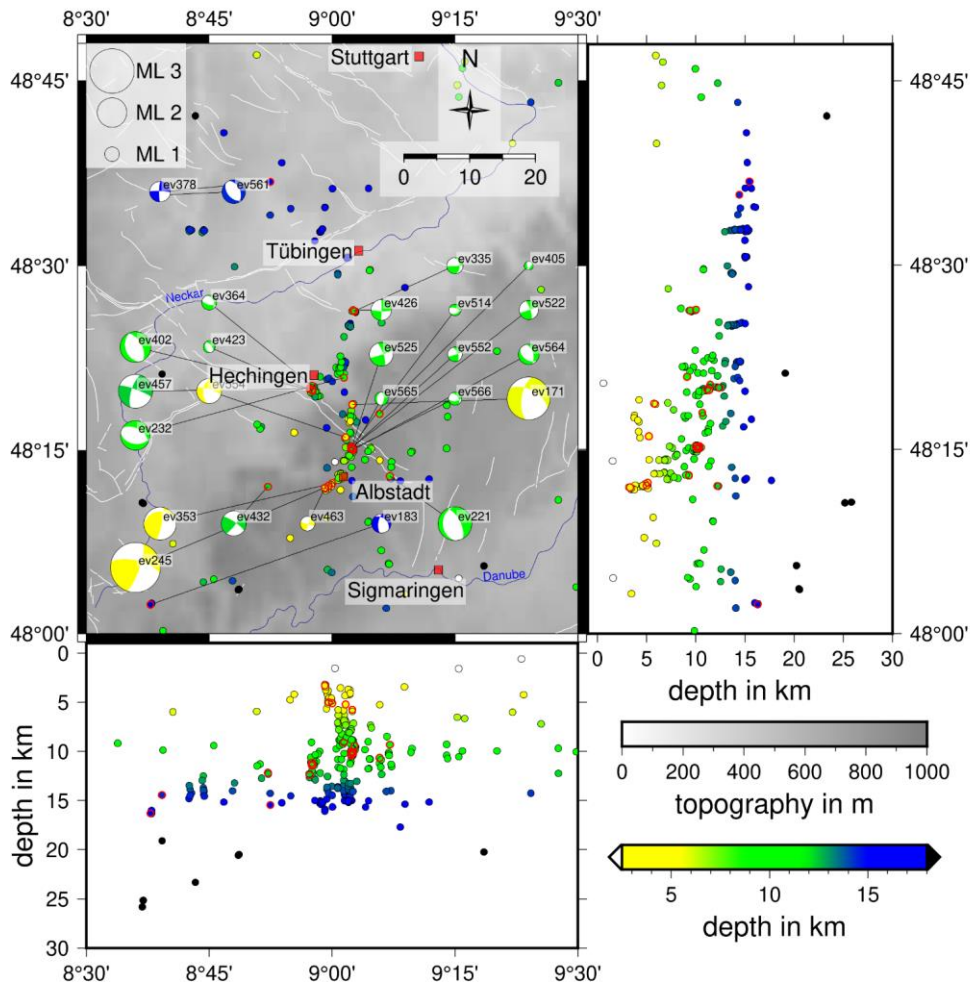
determined picks (Quality 0, Table A1), we consider the station delay times of MSS as practically zero. To account for similar
315 small station delay times and σ , we state that all station delay times in the range of -0.05 s to 0.05 s to be practically zero station delay times, if σ is greater than the actual station delay time (Fig. 6). The fact that the NLL station delay times of MSS and surrounding stations are close to zero indicates that, even though using a different and non-linear relocation algorithm for delay time estimation instead of VELEST, our determined minimum 1-D seismic velocity model ASZmod1 represents the seismic velocity structure below MSS and its surroundings very well.

320 We compared the relocated catalog with the original LED locations. Some events have large differences in hypocenter coordinates ($>0.1^\circ$ in latitude or longitude), which we identified as events with only a few arrival time picks (less than nine picks), a large azimuthal GAP (GAP $> 180^\circ$) or wrong phase picks. Furthermore, a large deviation of expectation and maximum likelihood hypocenters indicates an ill-conditioned inverse problem with a probable non-Gaussian distribution of the pdf (Lomax et al., 2000), which was the case for some events with only a few picked arrival times. Similar problems were also
325 identified by Husen et al. (2003), who compared NLL locations with the routine locations of the state earthquake service of Switzerland. They also found that a good depth estimate with NLL depends on the station distances to the earthquake. Especially, for events with many observations the depth estimate was worse if the closest station was further away than the focal depth of the event (Husen et al., 2003).

Our good located earthquakes are selected by the following criteria: more than eight travel time picks, a GAP less than 180° ,
330 a horizontal error estimate of less than 1 km, and a depth error estimate of less than 2 km (Fig. 7). Some of our good located events have quite different depth estimates compared to the LED solution (Fig. S45). Thus, we checked the station distribution for those events as proposed by Husen et al. (2003) and looked for wrong phase picks. Nevertheless, all these events have good phase picks, a small depth error estimate, evenly distributed stations and small deviations of expectation and maximum likelihood hypocenter coordinates. For this reason, we consider our new depth locations as well determined and reliable.

335 In comparison with the LED catalog the majority of our relocated earthquakes are characterized by a small eastward shift as well as a stronger clustering, especially in depth (Fig. S54). The latter may result from the handset depth location for some events of the LED.





340

Fig. 7 Hypocenters of the 337 best located events with a horizontal error of less than 1 km and a depth error of less than 2 km. Only events with a GAP smaller than 180° and more than eight travel time picks are included. Hypocenters are plotted as circles, color-coded with depth. All 2536 focal mechanisms are displayed also color-coded with depth, red circles indicate corresponding event hypocenter. The size of the focal mechanisms is scaled depending on ML of the event. Cluster codes are placed next to the fault

plane solutions. White lines indicate known and assumed faults (Regierungspräsidium Freiburg, Landesamt für Geologie, Rohstoffe und Bergbau (Hrsg.), 2019). Topography is based on the ETOPO1 Global Relief Model (Amante and Eakins, 2009).

4.4 Focal Mechanisms Models with FOCMEC

We determine fault plane solutions for 36-25 selected events with the program FOCMEC (Snoke, 2003); which conducts a grid search over the complete focal sphere and outputs all possible fault plane solutions. For this we used the P-polarity picks of the LED (Bulletin-Files des Landeserdbebendienstes B-W, 2018) and for events since 2016 we added P- and SH-polarities as well as SH/P amplitude ratios at the four AASN and three StressTransfer seismic stations. The local magnitude ML of those 36-25 events is in the range 0.90.6 to 3.43.4 (Table 2, Fig. 7, Bulletin-Files des Landeserdbebendienstes B-W, 2018).

To determine the SH/P amplitude ratios we only used SH- or P-picks with a quality of 2 or better and the SNR of the picked phase needed to be greater than 5. Furthermore, we compared the frequency content of the P- and SH-phase to assure that the waves have the same damping properties, and the the source process was simple (Snoke, 2003). If the determined frequency of P- and SH-phases differed by more than 5 Hz the SH/P amplitude ratio was omitted. All waveforms are instrument corrected and bandpass filtered between 1 Hz and 25 Hz. As FOCMEC uses the ratio on the focal sphere we need to correct our amplitudes for attenuation effects and phase conversion effects at the free surface (Snoke, 2003). To correct for attenuation effects we use Q_P and Q_S values determined by Akinci et al. (2004) for South Germany. The measured phase amplitude A depends on Q , the frequency of the phase f , the travelttime t and the amplitude A_0 at the source (e.g. Aki and Richards, 1980):

$$A = A_0 e^{-\pi \frac{ft}{Q}} \quad (1)$$

The correction factor for the free surface effect of SH waves is always two and independent of the incidence angle of the seismic wave. For the P wave the free surface correction strongly depends on the incidence angle and the v_p/v_s ratio (e. g. Aki and Richards 1980). We calculated the incidence angle for our P-phases of interest with the TAUP package of ObsPy (e.g. Beyreuther et al., 2010) using the AK135 model (Kennett et al. 1995) and find incidence angles in a range between 22.9° and 23.2° . As the variation between the incidence angles for the different station event combinations is very small we use for all events the median incidence angle of 23.05° . To calculate the v_p/v_s ratio, we use v_p and v_s of the second layer of our model ASZmod1 (Tabel 1), because in the first layer the velocities are considered to be unstable. After this correction the logarithm of the SH/P amplitude ratio is used as input in FOCMEC together with the P- and SH-polarities.

Due to small magnitudes and therefore a low signal to noise ratio of the waveforms, or due to the lower station coverage before 2016, we obtain only a small number of polarity picks or an unbalanced distribution of polarities on the foecal sphere. These adversities led to many uncertain fault plane solutions. For this reason, we combined events with similar hypocenter coordinates and polarity picks to determine a joint solution (Table 2). In this way we combined them to clusters with a corresponding cluster code (Table 2). The cluster code hints to the location of the events and increases from south to north. The cluster code C1 corresponds to clusters in the southern part of the ASZ close to Albstadt, whereas the cluster code C6 corresponds to events north of the river Neckar (Fig. 7). A subcode X (e.g. C1_1) subdivides clusters occurring in a specific

main cluster of the ASZ or in its vicinity. For example, C1_1 up to C1_4 are situated in the southern part of the ASZ and are all part of the cluster C1 (Fig. 7). We also determined a fault plane solution for one isolated single event, which is assigned the cluster code E1 (Table 2).

Kommentiert [SM1]: Amplitude ratios

To find the appropriate solution one can allow different types of errors in FOCMEC. We compare the relative weighting mode and the unity weighting mode of the FOCMEC inversion for all events. This is done to explore if the results differ significantly what could mean that they are questionable (Snoke, 2003). In the unity weighting mode each wrong polarity in the FOCMEC solution counts as an error of one. In the relative weighting mode, polarity errors near a nodal plane count less than polarity errors in the middle of a quadrant. Thus the polarity errors are weighted with respect to their distance to the nodal planes. This means a wrong polarity is weighted by the calculated absolute value of the radiation factor (ranging between 0 and 1). XXXXXXXXXXXX. (values for relative weighting) For both weighting modes we searched for solutions which allow increasing errors by varying systematically the different possible errors. Those errors are uncertainties in the P- and SH-polarities and the total error of wrong SH/P amplitude ratios, as well as the error range in which they are expected to be correct. For example, we might consider the unity weighting mode and an event with P- and SH-polarities. First, we check if we achieve a solution with zero errors for both. If no solution is found we increase the allowed errors for the SH-polarities to one, as the SH-polarities are more unsecure than the P-polarities. If still no solution is found we check for a wrong P-polarity and without wrong SH-polarity. This procedure is done for unity weighting and relative weighting and it is stopped if a solution is found. Furthermore, we checked for a dependency of the result on a single polarity, the next inversion runs for more errors are also determined by allowing more wrong polarity-picks than necessary to get a solution and compared the resulting solutions. Non-unique or problematic cases are excluded and here we only display fault plane solutions with a good stability in both cases.

Formatiert: Abstand zwischen asiatischem und westlichem Text anpassen, Abstand zwischen asiatischem Text und Zahlen anpassen

The output of FOCMEC results in a set of possible strike, dip, and rake combinations for each event. As preferred fault plane solution the one closest to the medians of strike, dip, and rake was chosen (Table 2, Fig. S6). We use the other possible solutions to determine uncertainties for our preferred fault plane solution. For this we recalculate all strikes into a range between 90° and 270°, to exclude not allow large differences in strike by the transition from 360° back to 0° and by the 180° ambiguity of the strike. We determine the 5% and 95% percentiles of strike, dip, and rake (Fig. S5) and calculate the width of the 5% to 95% percentile range (Δ strike, Δ dip, Δ rake, Table 3). These widths are taken as uncertainty ranges to account for a non-uniform solution distribution, as we observe it for example for the rake of cluster C6_1 (Fig. S5), and to assign a quality factor to the determined fault plane solutions (Table A2, Table 2). To get rid of non-unique or problematic cases the following restrictions are used: the median of the strike and dip of the unity and relative weighting modes has to be within a range of 15°, for the median of the rake must be within $\pm 20^\circ$, and the total allowed number of solutions is limited to 500. Furthermore, if the solutions yield a quality of 4 with Δ strike, Δ dip or Δ rake greater than 75°, then the fault plane solutions is omitted. Finally, all remaining fault plane solutions are inspected manually.

We observe a low quality (3 and 4) especially for ~~clusters consisting of only small magnitude~~ low magnitude events ($ML < 1.4$) and ~~without SH-polarities and SH/P ratios (Table 2)~~ clusters with a non-uniform station distribution on the focal sphere. In Fig. 7 the fault plane solutions are displayed scaled with magnitude and ~~their individual with event ID~~ cluster code.

ID	Time	M	$^{\circ}N$	$^{\circ}E$	Depth in km	P	S	SH	Strike in $^{\circ}$	Dip in $^{\circ}$	Rake in $^{\circ}$	Δ strike in $^{\circ}$	Δ dip in $^{\circ}$	Δ rake in $^{\circ}$	Strike(aux) in $^{\circ}$	Dip (aux) in $^{\circ}$	Rake (aux) in $^{\circ}$	Quality	
ev3 35	2016-04- 10T15:08	1. 1	48. 44	9. 05	9.44	8	3	0	353	43	-5	7.6	9.7	14. 5	87	87	-133	1	
ev3 53	2016-09- 02T07:58	2. 2	48. 20	9. 00	5.09	4	3	0	12	81	65	0.0	0.0	0.0	263	26	159	0	
ev3 64	2016-10- 13T01:54	1. 0	48. 34	8. 96	11.45	9	2	1	338	35	-43	46.1	0	50. 8	57. 8	105	67	-117	4
ev3 78	2016-12- 07T20:55	1. 4	48. 61	8. 87	15.46	8	2	2	181	82	-5	14.2	8	18. 8	68. 2	272	85	-172	4
ev4 02	2017-04- 15T17:16	2. 1	48. 33	8. 96	11.15	7	4	1	162	35	-81	0.0	0.0	0.0	331	55	-96	0	
ev4 05	2017-05- 07T15:19	0. 6	48. 30	9. 10	10.65	0	3	1	42	49	-41	56.8	4	35. 8	41. 8	162	60	-131	4
ev4 23	2017-07- 09T11:52	0. 8	48. 33	9. 96	11.36	8	4	0	158	37	-75	22.0	4	11. 6	29. 6	319	54	-101	2
ev4 26	2017-07- 23T13:48	1. 4	48. 44	9. 04	10.03	4	3	0	1	87	-10	0.0	0.0	0.0	92	80	-177	0	
ev4 32	2017-08- 27T06:00	1. 7	48. 20	8. 87	12.18	9	4	0	37	78	12	3.1	3	17. 3	7.6	304	78	168	1
ev4 57	2018-02- 10T12:44	2. 3	48. 33	8. 95	12.41	7	3	2	197	70	-9	2.0	6.9	0. 3	290	82	-160	1	
ev4 63	2018-03- 13T05:14	1. 0	48. 20	8. 99	3.30	1	3	1	15	79	-9	26.9	9	31. 3	63. 3	107	81	-169	4
ev5 14	2018-10- 15T18:46	0. 8	48. 25	9. 04	10.35	8	4	1	289	61	-65	23.3	5	15. 6	31. 6	65	38	-127	3
ev5 22	2018-10- 15T19:37	1. 3	48. 25	9. 04	10.00	7	4	3	341	76	-1	2.8	6.8	2. 10.	71	89	-166	1	
ev5 25	2018-10- 15T19:41	1. 6	48. 25	9. 04	10.08	7	4	4	341	75	-4	3.8	8.0	12. 0	72	86	-165	1	
ev5 52	2018-10- 17T03:02	1. 0	48. 25	9. 04	10.38	4	4	2	338	57	-7	9.3	0	32. 4	11. 4	72	84	-147	3
ev5 54	2018-10- 24T07:12	1. 7	48. 27	9. 03	5.22	3	4	2	185	50	-17	5.2	8	14. 0.6	286	77	-139	1	
ev5 61	2018-11- 18T16:23	1. 6	48. 60	8. 65	14.44	0	3	0	336	45	-78	22.0	4	25. 4	32. 4	139	46	-102	3
ev5 64	2018-11- 25T02:22	1. 4	48. 25	9. 04	10.20	5	3	2	344	53	-65	0.0	0.0	0.0	126	44	-119	0	
ev5 65	2018-11- 25T07:36	0. 9	48. 25	9. 04	10.24	1	2	0	190	35	-84	32.3	1	40. 2	12. 3	55	-94	4	
ev5 66	2018-11- 25T10:25	0. 9	48. 25	9. 04	10.22	3	5	1	323	50	-45	35.3	6	15. 5	14. 5	86	57	-130	3

hat formatiert: Schriftart: (Standard) Times New Roman, 10 Pt.

hat formatiert: Schriftart: (Standard) Times New Roman, 10 Pt.

hat formatiert: Schriftart: (Standard) Times New Roman, 10 Pt.

hat formatiert: Schriftart: (Standard) Times New Roman, 10 Pt.

hat formatiert: Schriftart: (Standard) Times New Roman, 10 Pt.

hat formatiert: Schriftart: (Standard) Times New Roman, 10 Pt.

hat formatiert: Schriftart: (Standard) Times New Roman, 10 Pt.

hat formatiert: Schriftart: (Standard) Times New Roman, 10 Pt.

hat formatiert: Schriftart: (Standard) Times New Roman, 10 Pt.

hat formatiert: Schriftart: (Standard) Times New Roman, 10 Pt.

hat formatiert: Schriftart: (Standard) Times New Roman, 10 Pt.

hat formatiert

ev1 71	2013-12- 04T19:42	2. 9	48. 31	9. 04	5.76	1 3	0	0	188	63	-39	11.4	41. 3	44. 7	298	56	-147	4
ev1 83	2014-01- 12T23:45	1. 3	48. 04	8. 63	16.29	1 2	0	0	187	64	-57	42.7	34. 9	37. 2	311	41	-138	4
ev2 21	2014-09- 09T00:46	2. 3	48. 21	9. 12	9.31	1 4	0	0	179	29	-67	47.3	59. 2	44. 8	333	64	-102	4
ev2 32	2014-10- 24T02:09	2. 0	48. 35	9. 02	9.11	1 1	0	0	300	51	-76	53.8	39. 9	38. 5	98	41	-107	4
ev2 45	2015-01- 28T00:05	3. 4	48. 20	8. 99	4.99	1 9	0	0	19	77	24	5.3	18. 5	61. 3	283	67	166	4

hat formatiert: Schriftart: (Standard) Times New Roman, 10 Pt.

hat formatiert: Schriftart: (Standard) Times New Roman, 10 Pt.

hat formatiert: Schriftart: (Standard) Times New Roman, 10 Pt.

hat formatiert: Schriftart: (Standard) Times New Roman, 10 Pt.

hat formatiert: Schriftart: (Standard) Times New Roman, 10 Pt.

Event-Origin-time	ML	Cluster-Code	P-Picks	SH-Picks	Longitude-in-°	Latitude-in-°	Depth-in-km
110624-1028	2	C3_1	11	0	9.04	48.31	7
131204-1941	2.9	C3_1	13	0	9.04	48.31	6
140518-0641	3	C1_4	16	0	8.99	48.20	5
171024-0209	2	C4_2	11	0	9.02	48.35	9
141031-1247	3.2	C1_4	15	0	8.99	48.20	4
150128-0004	3.4	C1_4	19	0	8.99	48.20	5
160203-2326	1.1	C5_1	7	2	9.05	48.44	10
160217-1925	1.7	C3_1	11	2	9.03	48.29	4
160309-0853	2.3	C1_1	13	2	9.01	48.22	6
160902-0757	2.2	C1_1	14	3	9.00	48.21	5
170415-1715	2.1	C4_2	17	4	8.96	48.33	11
170509-1618	2.8	C6_1	22	3	8.74	48.55	14
170510-2100	1	C6_1	10	3	8.74	48.55	14
170606-1327	1.8	C1_1	17	4	9.00	48.20	5
170606-2058	1.9	C1_1	25	4	9.00	48.20	5
170723-1348	1.4	C5_1	14	3	9.04	48.44	10
170827-0559	1.7	E1	29	2	8.87	48.20	12
171008-2254	1	C2_1	14	3	9.03	48.24	7
171104-2311	1	C6_2	13	3	8.98	48.55	15
171106-0039	1.4	C2_1	20	3	9.03	48.24	7
171212-0424	1.4	C1_2	17	2	8.99	48.20	4
171212-0539	2.2	C1_2	22	3	8.99	48.20	4
172323-2008	1	C1_3	15	3	8.99	48.20	3

Formatierte Tabelle

180210-1244	2.3	C4_1	27	3	8.95	48.33	12
180219-0829	1.3	C4_1	17	3	8.95	48.33	12
180221-0205	1	C4_1	13	3	8.95	48.33	12
180310-2116	2	C6_2	18	2	8.98	48.55	15
180313-0514	1	C1_3	11	3	8.99	48.20	3
180708-0438	1.1	C2_1	12	0	9.03	48.25	7
181015-1501	1.2	C2_2	18	3	9.04	48.25	10
181015-1937	1.3	C2_2	17	4	9.04	48.25	10
181015-1941	1.6	C2_2	27	4	9.04	48.25	10
181017-0301	1	C2_2	14	4	9.04	48.25	10
181125-0222	1.4	C2_3	25	3	9.04	48.25	10
181125-1026	0.9	C2_3	13	5	9.04	48.25	10
181213-1855	1.1	C4_1	18	6	9.02	48.38	12

Table 2 Parameters of the FOCMEC solutions. Values with (aux) refer to the assumed auxiliary plane. Events used for focal mechanism determination with corresponding local magnitude ML, cluster code, and number of used P- and SH-phase polarities, as well as hypocenter coordinates.

Parameters of the FCluster code	strike in°	dip in°	rake in°	Astrike in°	Adip in°	Arake in°	Strike in° (aux)	Dip in° (aux)	Rake in° (aux)	quality	Stress regime	S _{1max} orientation in°
E1	38	71	-5	0	4	2	129.63	85.27	-160.93	0	SS	175
C1_1	10	86	50	3	5	13	275.25	40.17	-173.79	1	U	132
C1_2	196	72	9	7	38	37	103.20	81.44	161.79	3	SS	148
C1_3	166	64	-16	15	39	41	263.16	75.66	-153.10	4	SS	123
C1_4	19	77	16	6	21	64	285.31	74.42	166.49	4	SS	153
C2_1	348	29	-29	15	10	18	316.27	51.98	-109.38	1	NF	110
C2_2	337	58	-26	6	14	5	123.52	87.05	-169.99	1	NS	117
C2_3	336	50	-57	18	9	23	81.49	68.18	-145.19	2	NF	133
C3_1	193	74	-20	5	30	26	103.86	76.41	-115.86	2	SS	151
C4_1	33	80	-3	4	11	18	288.73	70.81	-163.03	1	SS	169

hat formatiert: Schriftart: (Standard) +Textkörper (Times New Roman)

hat formatiert: Schriftart: (Standard) +Textkörper (Times New Roman)

hat formatiert: Schriftart: (Standard) +Textkörper (Times New Roman), 8 Pt.

Formatiert: Beschriftung

Formatierte Tabelle

Formatiert: Beschriftung

C4_2	166	42	-67	8	5	13	127.32	88.12	-159.99	1	NF	148
C5_1	5	64	-24	17	36	39	106.04	68.56	-151.90	3	SS	145
C6_1	180	80	-18	9	15	54	110.71	50.02	-122.99	4	SS	136
C6_2	218	70	2	14	24	34	273.23	72.28	-169.50	4	SS	174

Table 3 Selected fault plane solution for each cluster/event with corresponding uncertainty range, auxiliary fault plane, quality factor (Table A2), corresponding stress regime (see Sect. 4.5) and orientation of S_{Hmax}

Formatiert: Beschriftung

Formatiert: Beschriftung

Formatiert: Beschriftung

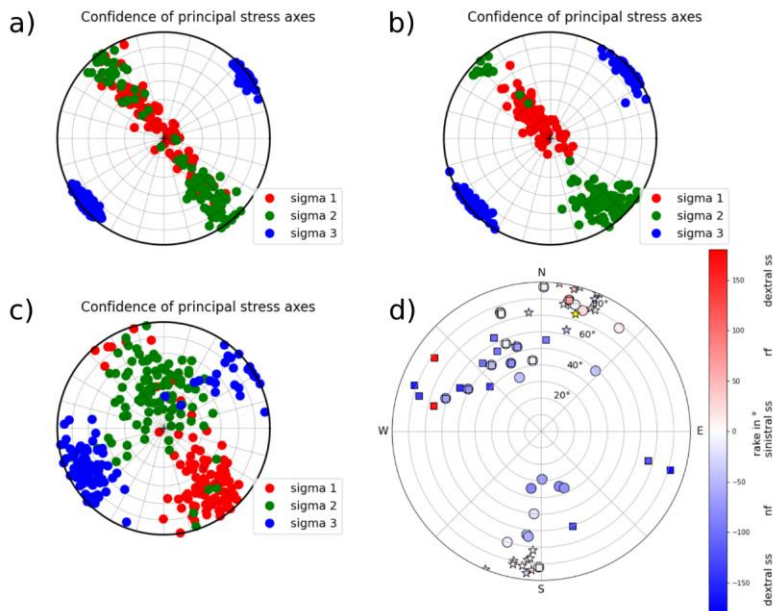
Formatiert: Beschriftung

Formatiert: Standard

Kommentiert [SM2]: Spannungsinversion

4.5 Direction of Maximum Horizontal Stress S_{Hmax} Stress Inversion

From our focal mechanisms we determined the directions of the maximum horizontal stress S_{Hmax} in our research area the principal stress axes σ_1 , σ_2 , σ_3 with the python code StressInverse (Vavryčuk, 2014). The algorithm runs a stress inversion after Michael (1984) modified to jointly invert for the fault orientations. To find the fault plane orientation Vavryčuk (2014) includes the fault instability I , which can be evaluated from the friction on the fault plane, the shape ratio R and the inclination of the fault planes relative to the principal stress axes. The input into StressInverse is the strike, dip and rake of our 25 fault plane solutions (Table 2). To achieve an accuracy estimate we allow 100 runs with random noise and define the mean deviation of our fault planes of 30° , which is reasonable considering a maximum Δ rake of 68.2° (Table 2). The friction is allowed to vary between 0.4 to 1 and R between 0 and 1. The stress inversion is calculated for three different input datasets: all 25 fault planes (Fig. 8a), only focal mechanisms with a depth greater than 7.5 km (20 fault planes, Fig. 8b) and focal mechanisms with a depth shallower than 7.5 km (5 fault planes, Fig. 8c). The selected azimuth and plunge of σ_1 , σ_2 and σ_3 are given in Table 3. The separation into two datasets was necessary due to a wide variation of the confidence levels of σ_1 and σ_2 along the NW-SE direction (Fig. 8a). With a separation into shallow and deep events, this variation is reduced, indicating a depth-dependency of the stress field (Fig. 8b). Nevertheless, due to the small amount of fault plane solutions in the depth range of 0.0 - 7.5 km we find higher scatter of the confidence of the three principal stress axes (Fig. 8c). The measured and predicted fault planes from the stress inversion are shown in Fig. 8d). The predicted fault planes are not changing for the different inversion runs. For this analysis we use the same conventions as used for focal mechanisms which are included in the World Stress Map (WSM, Zoback, 1992, Heidbach et al., 2016). We assign a stress regime (strike-slip (SS), normal faulting (NF), transverse faulting (TF), and mixed ones NS, TS) depending on the plunge of the pressure (P), tension (T), and B axis (Zoback, 1992). Depending on the stress regime, the direction of S_{Hmax} is either the P - or B -axis trend or the T -axis trend plus 90° (Table 3, for details see Zoback, 1992). This worked well for all clusters with the exception of cluster C1_1. For this cluster we are not able to derive a stress regime as all three axes have a moderate plunge in a range of 25° to 45° . In this case it is not possible to differ clearly between a maximum and minimum stress component (Zoback, 1992). For this reason, the P -axis trend is taken as S_{Hmax} direction of cluster C1_1 and it must be considered with care.



445 Fig. 8 a) Confidence plot of the principal stress axes σ_1 , σ_2 and σ_3 after the stress inversion of all fault plane solutions (Table 2) for the 100 different noise realizations.

b) Like Fig. 8a), but only for fault plane solutions with a depth greater than 7.5 km.

c) Like Fig. 8a), but only for fault plane solutions with a depth less than 7.5 km.

450 d) Strike, dip, and rake of all measured fault plane solutions (circles). Yellow star represents strike and dip of the 22 March 2003 earthquake (Stange and Brüstle, 2005). Other stars represent fault plane solutions calculated by Turnovsky (1981) for the earthquake series in 1978. Fault planes of StressInverse (Vavříček, 2014) are displayed by squares. Negative rake angles hint to normal faulting (nf) components and positive to reverse faulting (rf) components. Events with a rake close to zero exhibit sinistral strike-slip (sinistral ss) components, events with rake angles close to -180° or 180° hint to dextral strike-slip (dextral ss).

455

input	all fault planes		depth ≥ 7.5 km		depth < 7.5 km	
	azimuth	plunge	azimuth	plunge	azimuth	plunge
σ_1	360	81	332	67	149	47

Formatierte Tabelle

σ_2	140	7	140	22	343	42
σ_3	231	6	231	4	246	7
R	0.2		0.4		0.6	
friction	0.5		0.6		0.4	

Table 3 Result of the stress inversion for all events, deep events and shallow events. Azimuth and plunge angles in $^{\circ}$. R is the shape ratio.

All calculated S_{Hmax} directions are plotted together with the WSM data for our wider research area in Fig. 8. As most of our earthquakes have M_L smaller 2.5, the rock volume involved in the earthquake rupture is quite small. For this reason, we average the calculated trend of S_{Hmax} of all clusters to get one S_{Hmax} direction estimate for the area of the ASZ. This seems to be reasonable as in comparison with the WSM we find only minor deviations of the S_{Hmax} directions (Fig. 8). Furthermore, Rivera and Cisternas (1990) or Xu et al. (1992) demonstrated that composite solutions of stress field estimates from small earthquakes in a defined area represent a reliable regional stress field estimation. The median of the trend of S_{Hmax} is $147^{\circ} \pm 31^{\circ}$ at the ASZ. We use the 95% confidence range to give an error estimate. This results in an error of $\pm 31^{\circ}$. For later comparison we also calculated σ of S_{Hmax} , which is 20° .

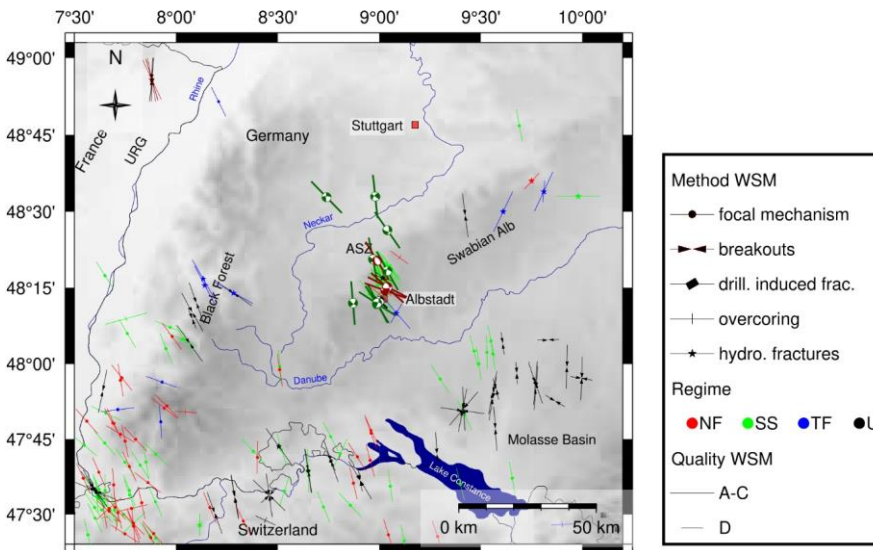


Fig. 8 Orientation of S_{Hmax} in the research area after the World Stress Map (WSM, light colors, Heidbach et al., 2016) and our new focal mechanisms and their corresponding S_{Hmax} (dark colors, thick lines), color-coded by stress regime (NF=normal

Formatiert: Standard

470 faulting, SS=strike slip, TF=transverse faulting, U=unknown). The WSM data is scaled by quality. Quality A-C indicates a
480 maximum error estimate of 25° (the good determined data), quality D of 40°. Topography is based on the ETOPO1 Global
Relief Model (Amante and Eakins, 2009).

Kommentiert [SM3]: Will be changed, also depending on the stress inversion results.

5 Results & Discussion

475 5.1 Velocity model and station delay times

The finally selected minimum 1-D seismic velocity model ASZmod1 consists of 5 layers (Fig. 4a and b). The layer boundaries are based on the seismic refraction interpretation of Gajewski et al. (1987). Layers with very similar seismic velocities were combined during the inversion process to keep the model as simple as possible (Occam's principle). The determined seismic velocities increase with depth and they are well constrained between 2.50 km and 18.25 km depth (Table 1). The layers between
480 -2.00 km to 2.50 km depth are not very stable due to the non-uniform distribution of rays and sources. Below 18.25 km depth we also have low resolution as all events used for inversion occur above. The comparison with the LED models gives a good agreement with both, the Swabian Jura and the Baden-Württemberg models (Fig. 4a). Our layer between 2.50 km and 5.60 km depth is in good agreement with the Swabian Jura model, whereas the deeper layer has a higher agreement with the Baden-Württemberg model (Fig 4a). The Swabian Jura model has a finer layering for the uppermost 2 km. We also used the Swabian
485 Jura model as input model for inversion, but due to the short horizontal raylength in comparison with the vertical raylength and the lack of events in the uppermost layers, the random seismic velocity starting models did not converge in the uppermost layers (Fig. 3), therefore we chose the very simple layering.

The v_p/v_s -ratio is between 1.67 and 1.75 for all layers and it decreases with depth. In comparison, the LED uses a constant v_p/v_s -ratio of 1.72 for Baden-Württemberg and 1.68 for the Swabian Alb, which agrees with our overall observed v_p/v_s -ratio
490 (Fig. 4b, Bulletin-Files des Landeserdbendienstes B-W, 2018). The higher v_p/v_s -ratio of 1.75 in the first layer is a result of the manually fixed seismic velocities during the inversion process. In the second layer the v_p/v_s -ratio is also 1.75 which may be caused by the numerical instability during the inversion of this layer and should be interpreted with care. In our best determined layers (layer 3 and 4) our model has similar v_p/v_s -ratios as the Swabian Jura model of the LED (Fig. 4b, Bulletin-Files des Landeserdbendienstes B-W, 2018).

495 The station delay times of the P- and S-waves have a simple pattern of increasing delay times with distance to reference station MSS (Fig. 6). Their very low values in the area of the ASZ demonstrate that the v_p and v_s distributions of ASZmod1 very well represent the true seismic velocities in this area. Around the ASZ, the central Swabian Alb and the Molasse Basin are characterized by positive station delay times, thus slower seismic velocities along the propagation paths relative to ASZmod1. Other areas like the Black Forest exhibit negative delay times, so faster seismic velocities than ASZmod1.

500 The lateral seismic velocity contrasts of the different near-surface layers of Baden-Württemberg are small in comparison with our station delay times. For this reason, we compare our station delay times with the lateral depth variations of the crystal line

basement to find a possible relationship. The basement depth is described by the 3-D geological model of the Geological Survey of Baden-Württemberg (Rupf and Nitsch, 2008). Based on this model we estimate the vertical travel time at all our recording stations with more than either 5 P- or S-phase travel time picks using the seismic velocities of the first layer in ASZmod1 from the basement top to each recording station. For these values we calculated the travel time differences of all stations relative to station MSS and compared the results (Fig. 9) with our real station delay times (Fig. 6). As result we find that the calculated travel time differences due to basement depth variations correlate to more than 85% with our station delay times. Hence, basement depth variations are the main reason for the observed station delay times in our study region. The remaining 15% of the station delay time terms may be explained by non-vertical ray path effects and lateral variations in seismic velocity due to different near-surface rock types. Furthermore, other lateral heterogeneities like dipping or wave guiding layers may influence the station delay times as well.

Comparison of NLL and estimated sdt relative to MSS for:
P-wave, correlation coefficient is 0.86
S-wave, correlation coefficient is 0.91

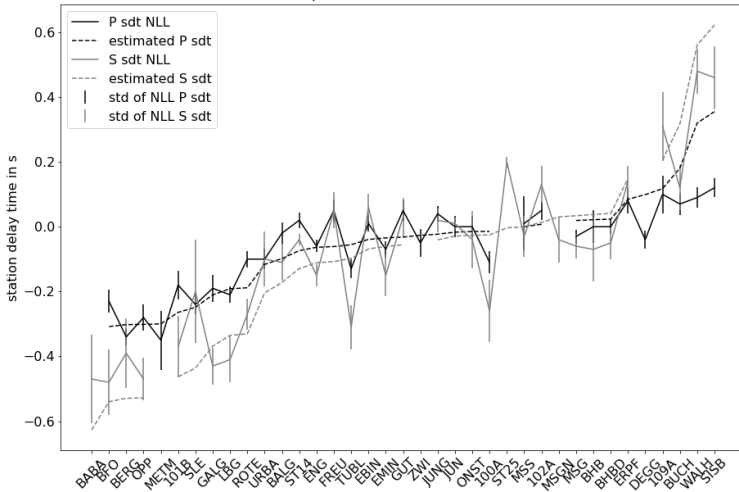
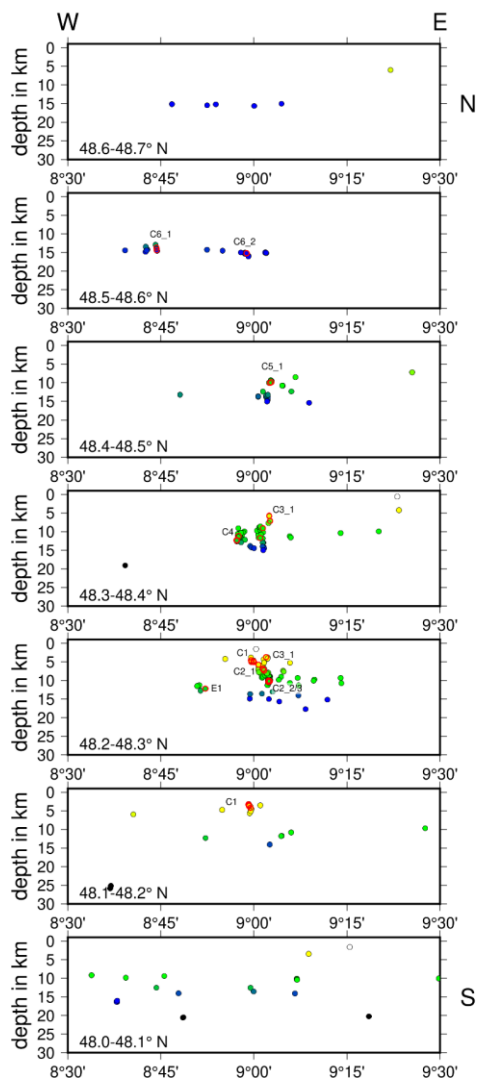
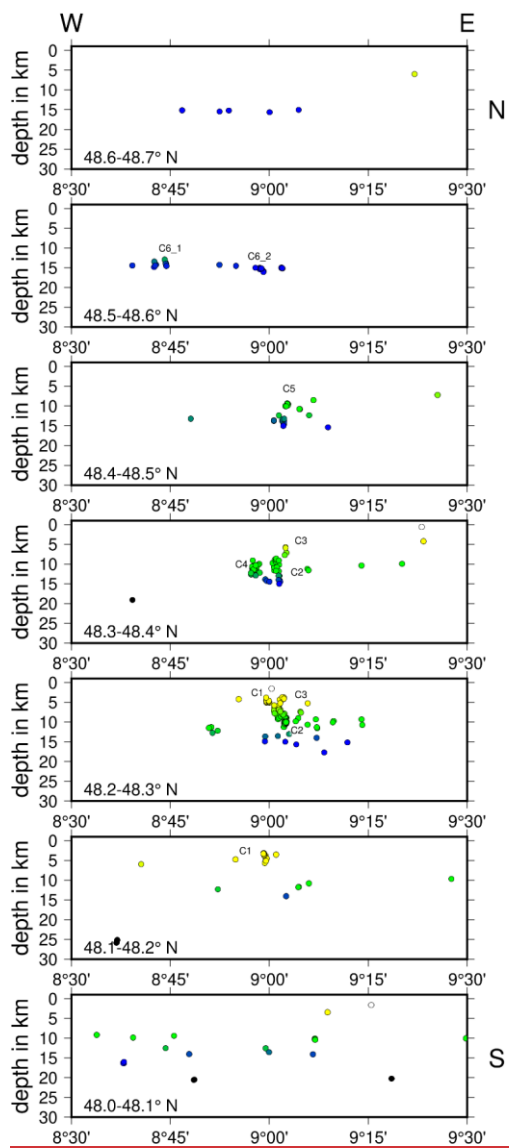
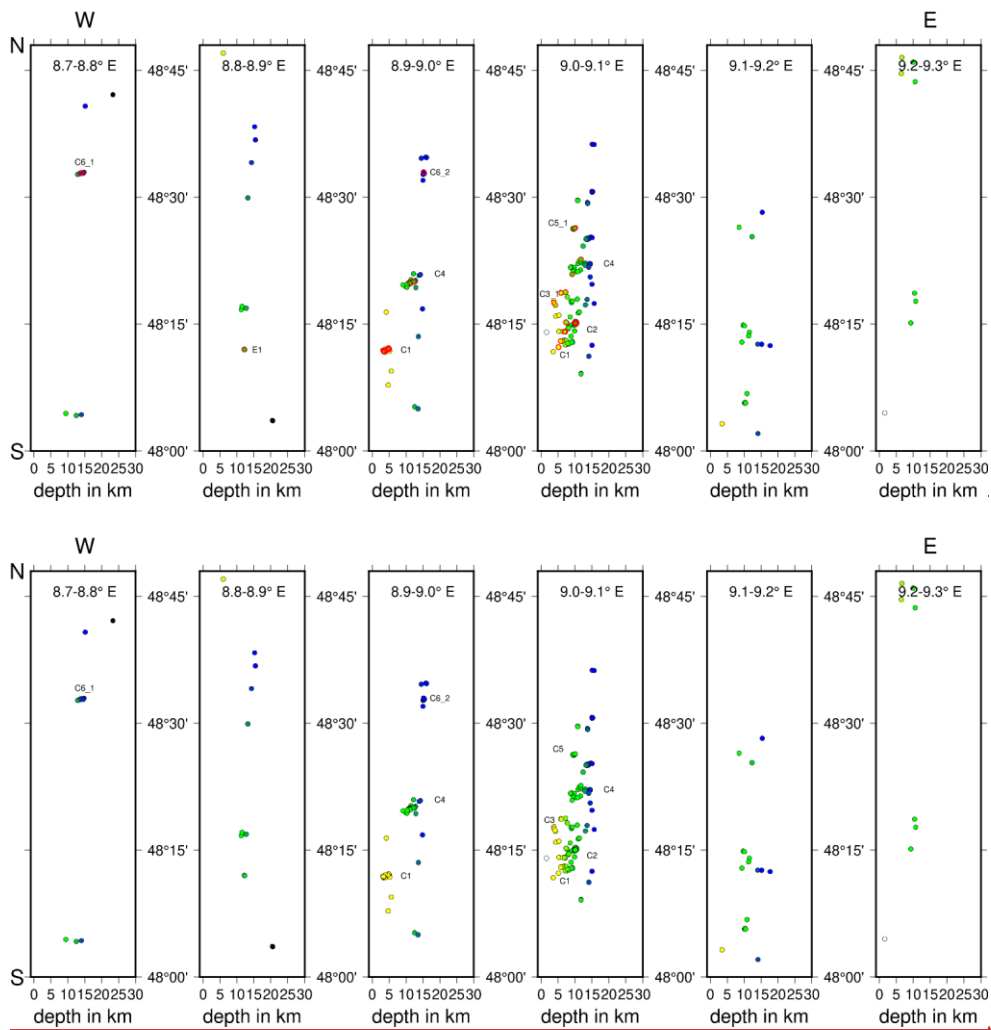


Fig. 9 Comparison of NLL station delay times (sdt) and estimated station delay times due to depth variations of the crystalline basement. P-waves (black) and S-waves (gray). Stations along the x-axis are sorted from shallow to deep crystalline basement model depth.





520 Fig. 10 Seismicity distribution of the ASZ from north (top) to south (bottom). Circles indicate hypocenters in the corresponding slice, color-coded with depth_ (as in Fig. 7), [cluster codes for orientation](#).



hat formatiert: Deutsch (Deutschland)

Fig. 11 Seismicity distribution of the ASZ from west (left) to east (right). Circles indicate hypocenters in the corresponding slice, color-coded with depth (as in Fig. 7). [cluster codes for orientation](#).

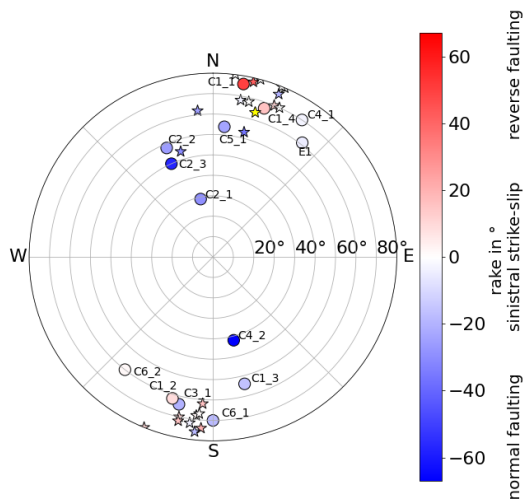
5.2 Seismicity and fault plane solutions of the ASZ

530 The seismicity of the ASZ (Fig. 7) aligns almost north-south. Our relocated earthquakes occur in a depth range of 1 km to 18 km. If we follow the seismicity distribution from south to north, the minimum hypocenter depth increases from around 3 km to 5-14 km. Earthquakes below 18 km depth are rare at the ASZ. The top of the lower crust is at about 18-20 km depth (Gajewski and Prodehl, 1985, Aichroth et al., 1992), therefore, seismicity is concentrated in the upper crust. The hypocenters can be separated in several fault segments. This segmentation gets more obvious if we analyze east-west and north-south slices (Fig. 10 & 11). In the north of the river Neckar (48.5-48.7° N), mainly deep (around 15 km depth) earthquakes occur, which can be separated into two clusters, one at 8.75 °E (C6_1-4) and one at 8.95 °E (C6_2-2, Fig. 10). Between the river Neckar and the town of Hechingen (48.3-48.5° N) we observe seismicity in the depth range of 5-15 km. There are three separate clusters, one west of 9 °E, directly south of Hechingen (C4), and two clusters east of 9 °E (C5-4 and C3-4). Near the town Albstadt (48.2-48.3° N) the seismicity occurs across the whole seismically active depth range (1.5–18 km). Most seismicity happens between 9 °E and 9.1 °E (C2, C3-4). In 2 km to 8 km depth we find a small seismicity cluster southwest of Albstadt (8.9-9.0° E, C1). This cluster can be traced southward to 48.2 °N (48.1-48.2° N, C1).

545 Most of the fault plane solutions are characterized by the typical NNE-SSW strike of the ASZ, but we also observe some events with NNW-SSE strike (Fig. 7, Fig. 8d, Table 2). The most events with a strike of NNE-SSW are characterized by steep fault planes (dip angle greater 60°) and rake angles around 0°, hinting to sinistral strike-slip. This is the typical or main faulting mechanism of the ASZ (Fig. 8d, Turnovski, 1981, Stange and Brüstle, 2005). We also observe one event with NNE-SSW strike with a clear reverse faulting component and a steep fault plane of 86° (Fig. 8d). The other events with NNE-SSW strike and the events with NNW-SSE strike have lower dip angles (smaller 60°) and mainly negative rake angles, hinting to normal faulting (Fig. 8d). The here observed faulting behaviors can all be explained by a compressional stress regime with an average horizontal stress orientation of around 150° (Müller et al., 1992, Reinecker et al., 2010, Heidbach et al., 2016) acting on either the NNE-SSW or NNW-SSE oriented fault planes. The stress inversion after Vavryčuk (2014) also inverts for the probable rupturing fault plane in the current stress field (Fig. 8d). By comparing strike, dip and rake of the fault planes of the events in Table 2, with the probable fault plane of StressInverse, we observe that the NNW-SSE oriented fault planes – typical for the ASZ - changed to their auxiliary fault planes, so dextral strike-slip with a strike of WNW-ESE (Fig. 8d). As the aftershock distribution of the stronger events is NNE-SSW (e.g. Stange and Brüstle 2005) as well as our relocated events in Fig. 7, of course a sinistral fault plane with NNE-SSW strike is the preferred one. As explanation for this discrepancy we suggest that the ASZ is an inherited weak structure which needs much less stress for failure than the more probable oriented WNW-ESE oriented fault planes predicted by StressInverse. Ring et al. (2020) find that the ASZ coincides with the NNE-SSW oriented boundary fault between of the Triassic-Jurassic Spaichingen high and the Mid-Swabian basin, also hinting to a preexisting structure.

hat formatiert: Schriftfarbe: Text 1

560 The earthquake cluster C4 south of Hechingen (Fig. 10 & 11) consist of events with normal faulting components (ev402,
 ev423, ev364) and the strike-slip event ev457 (Fig. 7). This cluster aligns along the boundary faults of the HZG and the events
 strike almost parallel to the HZG (Fig.7, 8d). Other earthquakes close to the HZG boundary fault strike also almost parallel to
 the HZG (e.g. ev552, ev566, ev564). Most of the fault-plane solutions are characterized by the typical NNE-SSW strike of the
 ASZ, but we also observe some events with NNW-SSE strike (Fig. 7). Furthermore, most of the dip angles are greater than
 565 60°, indicating a steep fault plane (Fig.12). If the rake angle is close to zero it indicates sinistral strike-slip faulting, if it is close
 to -180° or 180° it indicates dextral strike-slip faulting. Negative rake angles smaller than zero and greater than -180° imply
 normal faulting components, whereas positive rake angles imply reverse faulting components. Here, the events with a lower
 dip angle have a higher angle in rake, hinting to normal faulting components for negative rake angles and reverse faulting
 components for positive rake angles. The events with a rake close to zero indicate sinistral strike-slip components, which is
 570 the typical faulting mechanism of the ASZ (e.g. Turnovski, 1981, Stange and Brüstle, 2005). Comparing the fault plane
 solutions determined by Turnovski (1981) and the fault plane solution of the 22nd March 2003 earthquake (Stange and Brüstle,
 2005) with our newly determined fault plane solutions we observe very similar dominating faulting mechanisms (Fig. 12).



575 Fig. 12 Strike, dip, and rake of all measured fault plane solutions with corresponding cluster code. Yellow star represents strike
 and dip of the 22nd March 2003 earthquake (Stange and Brüstle, 2005). Other stars represent fault plane solutions calculated
 by Turnovski (1981) for the earthquake series in 1978. Negative rake angles hint to normal faulting components and positive

Formatiert: Standard

to reverse faulting components. Events with a rake close to zero exhibit sinistral strike-slip components. Colorbar is scaled by minimum and maximum rake angle.

580 The normal faulting events (cluster C2, C4_2) have a strike of around 160°, almost parallel to the around NW-SE striking HZG, and they are mainly located close to the boundary faults of the HZG (Fig. 7). The depth extension of the HZG is not well known but estimated from its extensional width and its dip angles of the main boundary faults at the surface. Based on these parameters, the boundary faults are thought to converge in about 2-3 km depth (Schädel, 1976). The faulting pattern of events close to HZG may indicate that the HZG boundary faults reach to greater depth as already suggested by Schädel (1976) or Illies (1982). This may also imply that ev457 is a dextral strike-slip event, like suggested by the result of the stress inversion. Relative event locations may help to identify the active fault planes in more detail using more data in future work.

585 To test if the HZG boundary faults may relate to the events in 7-11 km depth we projected the faults of the fault plane solutions (both fault plane and auxiliary plane, Table 3) to the surface (Fig. S6). For most of our fault plane solutions we cannot differ clearly if the fault plane or the auxiliary plane is the active fault plane as we only have few events available. In case of our cluster C2_2 we can clearly see a lineation of the earthquake hypocenters of the swarm in October 2018 along the strike with the fault plane in NNW direction. Nevertheless, this projected fault plane does not correlate with the strike of the HZG but is slightly oblique to it. The cluster C4 close to Hechingen has a higher correlation of the auxiliary fault planes with the strike of the HZG if the faults are projected for each event separately within the cluster to the surface (Fig. S7, auxiliary fault planes: C4_1, strike 289°, C4_2, strike 127°, HZG, strike 130°, Baumann, 1986). If the auxiliary fault planes were the active fault planes, then cluster C4_1 would hint to dextral strike-slip movement and cluster C4_2 to reverse faulting at the northern HZG boundary fault. This faulting pattern may indicate that the HZG boundary faults reach to greater depth as already suggested by Schädel (1976) or Illies (1982). However, we cannot clearly distinguish between the two possible fault planes as the seismicity is still distributed too diffuse.

5.3 Stress field around the ASZ

600 We inverted from our fault plane solutions, we for the direction of the principal stress axes σ_1 , σ_2 , σ_3 (Table 3). As for a combined run the differentiation between σ_1 and σ_2 is difficult (Fig. 8a), we also inverted a split data set separated by the depth of 7.5 km (Fig. 8b,c). For depths shallower than 7.5 km we observe the horizontal maximum stress S_{Hmax} with an azimuth of 149° to be greater than than the vertical stress S_V (Table 3). For a depth range greater than 7.5 km we observe $S_V > S_{Hmax}$. estimate The depth dependence of the relative stress magnitudes is also known from other sites in the region. In the deep boreholes in Soultz (Central Upper Rhine Graben), $S_V > S_{Hmax}$ is found in the upper ca. 2.5 km. Below $S_{Hmax} > S_V$ is valid to at least 5 km depth (Valley & Evans, 2003). Here S_{Hmax} has a direction of N169°E±14°. In the southern Upper Rhine Graben, Plenefisch and Bonjer (1997) determined $S_{Hmax} > S_V$ in the upper crust to 15 km depth, whereas $S_V > S_{Hmax}$ was determined in the lower crust (>15 km depth) from fault plane solutions. Our results indicate a shallower level (~7 km) for the

change of the maximum stress components which may be due to a change in the rock rheology and needs to be studied with more data.

~~Our the averaged~~ direction of S_{Hmax} ~~is~~ 140° - 149° ~~be~~ $147^{\circ} \pm 31^{\circ}$ ($\sigma = 20^{\circ}$). The orientation of S_{Hmax} for southwest Germany is estimated to be around 150° with a σ of 24° (Reinecker et al., 2010) and for whole Western Europe 145° with a σ of 26° (Müller et al., 1992), which are both in agreement with our local S_{Hmax} orientation. Houlié et al. (2018) also observes a similar stress field in east Switzerland, southeast of our research area. ~~Furthermore, we find also a good coincidence with the single~~ S_{Hmax} ~~orientations of our clusters in comparison with the WSM (Fig. 8).~~ Reinecker et al. (2010) suggest the gravitational potential energy of the Alpine topography as main source of the local stress field because the stress field orientation in the northern Alpine foreland is always perpendicular to the Alpine front. Kastrup et al. (2004) also observe a change of stress field orientation with the Alpine front for the northern Alpine foreland in Switzerland. They explain the change of the orientation of the minimum horizontal stress S_1 parallel to the Alpine front with a perturbation of the regional European stress field due to the indentation of the Adriatic Block. Müller et al. (1992) identify the plate driving forces as sources of the maximum compression in NW to NNW direction for whole western Europe, only perturbed by large geological structures like the Alps. As our study area is quite small, we cannot observe major lateral stress variations, however, the good coincidence with the regional stress field (Müller et al., 1992, Reinecker et al., 2010) is a strong indication that the driving tectonic forces of the seismicity of the ASZ are the regional plate driving forces combined with the Alpine topography. Small scale stress perturbations and variations of faulting mechanisms (Fig. 7 and 8) may be due to local heterogeneities of crustal material causing variations in rigidity or preexisting structures. These factors may also play a role in the segmentation of the ASZ which will be analyzed in more details in the next years.

6 Conclusion and Outlook

We used our newly complemented seismicity catalog to invert for a robust new minimum 1-D seismic velocity model with station delay times for the ASZ region. These station delay times can be explained by the depth variation of the crystalline basement in the upper crust of Baden-Württemberg (Fig. 9). The relocated seismicity of the years 2011 to 2018 pictures the ASZ as a complex fault structure, with its current main active focus between the cities Albstadt and Tübingen on the Swabian Alb. The hypocenter error estimates clearly become smaller for events after 2016 due to the densified seismic station network of the LED and the complementing AASN stations. Thus, we expect another improvement and an increase in detectable events from 2019 onwards due to our additionally installed StressTransfer stations (Fig. 1). Future work will take advantage of the densified seismic station network and focus on small magnitude event detection based on template matching in the area of the ASZ.

Most of the seismicity takes place in a N to S oriented band east of 9° E (Fig. 7). A spatial clustering of events is found which may indicate separate fault planes. If such a separation can be verified in the future, this segmentation would limit the maximum size of earthquake rupture planes and its related hazard potential (Grünthal and the GSHAP Region 3 Working Group, 1999).

Nevertheless, we find the shallow cluster C1 slightly separated to the west from the other events, as well as the deeper cluster C4 near Hechingen. Furthermore, we observeThe clusters C2 and C4_2 are clear normal faulting events, which were so far not observed for the ASZ. A relation of the clusters C4_1 and C4_2 with a continuation of the HZG into the crystalline basement is possible and needs further observational constraints to better describe the seismic potential of the HZG—as indicated by our fault line projections. Ongoing work will determine relative locations for all events from 2016 and following years to obtain an even sharper image of the fault planes of the ASZ. We also continue complementing our catalog with new earthquakes and fault plane solutions after 2018.

The estimated S_{Hmax} has a NNW-SSW trend. This is in good agreement with other studies (Müller et al., 1992, Kastrup et al., 2004, Reinecker et al., 2010, Houlié et al., 2018). As plausible driving forces of our local stress field, we identify the regional plate driving forces as well as the Alpine topography (Müller et al., 1992, Kastrup et al., 2004, Reinecker et al., 2010). In the upper part of the crust S_{Hmax} exceeds SV (Fig. 8). Below about 7–8 km depth SV seems to be the dominating stress component. To get a better estimate of the stress field around the ASZ we plan to invert our fault plane solutions to determine the whole stress field tensor. Furthermore, within the StressTransfer project similar investigations are planned for the URG to the west and the Molasse Basin south-east of the ASZ, to get a better understanding of the stress field in the northern Alpine foreland of southwest Germany.

hat formatiert: Tiefgestellt

Appendix

Pick time uncertainties	lp-ep <= 0.05 s	0.05 s < lp-ep <= 0.1 s	0.1 s < lp-ep <= 0.2 s	0.2 s < lp-ep <= 0.4 s	lp-ep > 0.4s
Quality	0	1	2	3	4

Table A1 Definition of the error quality relationship. lp-ep represents the time window in which the final pick is manually selected.

	$\Delta x \leq 10^\circ$	$10^\circ < \Delta x \leq 20^\circ$	$20^\circ < \Delta x \leq 30^\circ$	$30^\circ < \Delta x \leq 40^\circ$	$40^\circ < \Delta x$
Quality	0	1	2	3	4

Table A2 Classification of the qualities used for focal mechanisms. Δx represents $\Delta strike$, Δdip and $\Delta rake$. The lowest quality of all three parameters is given to the fault plane solution.

665 **Code availability**

The preprocessing and picking analyses of the data were done in Python with the open-source toolbox ObsPy (Beyreuther et al., 2010, <https://github.com/obspy/obspy/wiki>). For further data analyses we used the freely available programs VELEST (Kissling et al., 1994, Kissling et al., 1995, VELEST Version 4.5, <https://seg.ethz.ch/software/velest.html>), NonLinLoc (Lomax et al., 2000, <http://alomax.free.fr/nlloc/index.html>) and FocMec (Snoke 2003, <http://ds.iris.edu/pub/programs/focmec/>) and StressInverse (Vavryčuk, 2014, <https://www.ig.cas.cz/en/stress-inverse/>). All figures were created with either the matplotlib library in Python (<https://matplotlib.org/>) or the Generic Mapping Tools (GMT, Wessel et al., 2019, <https://www.generic-mapping-tools.org/>).

Data availability

We used the restricted Bulletin-Files of the state earthquake service of Baden-Württemberg (LED), which were provided to us by the LED (Bulletin-Files des Landeserdbendienstes B-W, 2018, https://lgrb-bw.de/erdbeben/index_html?lang=1). We analyzed the data of four AlpArray stations of the Z3 network, which will become available on 1st April 2022 to people outside the AlpArray Working Group (http://www.alparray.ethz.ch/en/seismic_network/backbone/data-access/). The data of the StressTransfer Network is currently restricted and will become available on 1st April 2022.

Team list

680 The complete member list of the AlpArray Working Group can be found at <http://www.alparray.ethz.ch>.

Author contribution

Sarah Mader carried out the fieldwork, analyzed the data with self-written and open-source programs and prepared the manuscript and figures. Joachim Ritter and Klaus Reicherter formulated the project, obtained funding and started the fieldwork. All three were involved in writing the manuscript. The AlpArray Working Group organized and coordinated the AlpArray Seismic Network operation.

Competing interests

The authors declare that they have no conflict of interest.

Acknowledgments

We thank the State Earthquake Service of Baden-Württemberg (Landeserdbebendienst B-W) for providing waveform data, pick files and internal information (Az4784/18_3303). We thank Andrea Brüstle, Tobias Diehl, and Dietrich Lange for programming and program related support and helpful discussions. Waveform recordings were provided by the AlpArray Seismic Network (2015). Recording instruments were provided by the Karlsruhe BroadBand Array, Karlsruhe Institute of Technology. S.M. and J.R. were supported by the Deutsche Forschungsgemeinschaft (DFG) by grant RI1133/13-1 and K.R. by grant RE1361/31-1 within the framework of DFG Priority Programme “Mountain Building Processes in Four Dimensions (MB-4D)” (SPP 2017). Felix Bögelspacher, Felix Pappert, [Leon Merkel](#), [Sergio León-Ríos](#) and Werner Scherer assisted the fieldwork. Michael Frietsch helped with the data management. We thank numerous people and associations for supporting the installation of the mobile recording instruments on their land. We acknowledge support by the KIT-Publication Fund of the Karlsruhe Institute of Technology.

We thank the AlpArray Seismic Network Team: György HETÉNYI, Rafael ABREU, Ivo ALLEGRETTI, Maria-Theresia APOLONER, Coralie AUBERT, Simon BESANÇON, Maxime BÈS DE BERC, Götz BOKELMANN, Didier BRUNEL, Marco CAPELLO, Martina ČARMAN, Adriano CAVALIERE, Jérôme CHÈZE, Claudio CHIARABBA, John CLINTON, Glenn COUGOULAT, Wayne C. CRAWFORD, Luigia CRISTIANO, Tibor CZIFRA, Ezio D’ALEMA, Stefania DANESI, Romuald DANIEL, Anke DANNOWSKI, Iva DASOVIĆ, Anne DESCHAMPS, Jean-Xavier DESSA, Cécile DOUBRE, Sven EGDORF, ETHZ-SED Electronics Lab, Tomislav FIKET, Kasper FISCHER, Wolfgang FRIEDERICH, Florian FUCHS, Sigward FUNKE, Domenico GIARDINI, Aladino GOVONI, Zoltán GRÁCZER, Gidera GRÖSCHL, Stefan HEIMERS, Ben HEIT, Davorka HERAK, Marijan HERAK, Johann HUBER, Dejan JARIĆ, Petr JEDLIČKA, Yan JIA, Hélène JUND, Edi KISSLING, Stefan KLINGEN, Bernhard KLOTZ, Petr KOLÍNSKÝ, Heidrun KOPP, Michael KORN, Josef KOTEK, Lothar KÜHNE, Krešo KUK, Dietrich LANGE, Jürgen LOOS, Sara LOVATI, Deny MALENGROS, Lucia MARGHERITI, Christophe MARON, Xavier MARTIN, Marco MASSA, Francesco MAZZARINI, Thomas MEIER, Laurent MÉTRAL, Irene MOLINARI, Milena MORETTI, Anna NARDI, Jurij PAHOR, Anne PAUL, Catherine PÉQUEGNAT, Daniel PETERSEN, Damiano PESARESI, Davide PICCININI, Claudia PIROMALLO, Thomas PLENEFISCH, Jaroslava PLOMEROVÁ, Silvia PONDRELLI, Snježan PREVOLNIK, Roman RACINE, Marc RÉGNIER, Miriam REISS, Joachim RITTER, Georg RÜMPKER, Simone SALIMBENI, Marco SANTULIN, Werner SCHERER, Sven SCHIPPKUS, Detlef SCHULTE-KORTNACK, Vesna ŠIPKA, Stefano SOLARINO, Daniele SPALLAROSSA, Kathrin SPIEKER, Josip STIPČEVIĆ, Angelo STROLLO, Bálint SÜLE, Gyöngyvér SZANYI, Eszter SZŰCS, Christine THOMAS, Martin THORWART, Frederik TILMANN, Stefan UEDING, Massimiliano VALLOCCHIA, Luděk VECSEY, René VOIGT, Joachim WASSERMANN, Zoltán WÉBER, Christian WEIDLE, Viktor WESZTERGOM, Gauthier WEYLAND, Stefan WIEMER, Felix WOLF, David WOLYNIEC, Thomas ZIEKE, Mladen ŽIVČIĆ and Helena ŽLEBČÍKOVÁ.

[The manuscript was improved by helpful comments from T. Plenefisch and an anonymous reviewer.](#)

720 **References**

Aichroth, B., Prodehl, C. and Thybo, H.: Crustal structure along the Central Segment of the EGT from seismic-refraction studies, *Tectonophysics*, 207, 43-64, 1992.

[Aki, K. and Richards, P. G. \(2002\): *Quantitative Seismology: Theory and Methods*, W.H. Freeman, San Francisco, CA, Second Edition.](#)

[Akinci, A., Mejia, J., & Jemberie, A. L. \(2004\). Attenuative dispersion of P waves and crustal Q in Turkey and Germany. *pure and applied geophysics*, 161\(1\), 73-91.](#)

hat formatiert: Deutsch (Deutschland)

730 AlpArray Seismic Network (2015): AlpArray Seismic Network (AASN) temporary component. AlpArray Working Group. Other/Seismic Network, https://doi.org/10.12686/alparray/z3_2015, 2015.

Amante, C. and Eakins, B.W.: ETOPO1 1 Arc-Minute Global Relief Model: Procedures, Data Sources and Analysis. NOAA Technical Memorandum NESDIS NGDC-24. National Geophysical Data Center, NOAA, 2009.

[Asch, K., 2005. The 1:5 Million International Geological Map of Europe and Adjacent Areas. BGR \(Hannover\), 1 map.](#)

Becker, A.: An attempt to define a "neotectonic period" for Central and northern Europe, *Geologische Rundschau*, 82, 67–83, 1993.

740 Beyreuther, M., Barsch, R., Krischer, L., Megies, T., Behr, Y. and Wassermann, J.: ObsPy: A Python Toolbox for Seismology, *SRL*, 81(3), 530-533, <https://doi.org/10.1785/gssrl.81.3.530>, 2010.

[Bonjer, K.-P.: Seismicity pattern and style of seismic faulting at the eastern borderfault of the southern Rhine Graben. *Tectonophysics*, 275, 41-69, 1997.](#)

hat formatiert: Deutsch (Deutschland)

Bulletin-Files des Landeserdbendienstes B-W, Ref. 98 im Landesamt für Geologie, Rohstoffe und Bergbau im Regierungspräsidium Freiburg (<http://www.lgrb-bw.de>); Az4784/18_3303, 2018.

750 Diehl, T., Kissling, E. and Bormann, P.: Tutorial for consistent phase picking at local to regional distances. In: Bormann, P. (Ed), *New Manual of Seismological Observatory Practice 2 (NMOSOP-2)*, Potsdam: Deutsches Geoforschungszentrum GFZ, pp 1.21, 2012.

755 Gajewski, D. and Prodehl, C.: Crustal structure beneath the Swabian Jura, SW Germany, from seismic refraction investigations. *Journal of Geophysics*, 56(2), 69-80, 1985.

Gajewski, D., Holbrook, W. S. and Prodehl, C.: A three-dimensional crustal model of southwest Germany derived from seismic refraction data. *Tectonophysics*, 142, 49-70, 1987.

760 Geyer, O.F. and Gwinner, M.P.: *Geologie von Baden-Württemberg*, 5th revised edition by Geyer, M., Nitsch, E. and Simon, T., Schweitzerbart, Stuttgart, 2011.

Gräber, F.: *Lokalbebtomographie mit P-Wellen in Long Valley, Kalifornien, und die Möglichkeiten einer Anwendung im südlichen Rheingraben*. Diplomarbeit, Geophysical Institute, TU Karlsruhe and Institute of Geophysics, ETH Zürich, 1993.

765

Grünthal, G. and the GSHAP Region 3 Working Group: Seismic hazard assessment for Central, North and Northwest Europe: GSHAP Region 3. *Anali di Geofisica*, 42 (6), 999-1011, 1999.

770 Haessler, H., Hoang-Trong, P., Schick, R., Schneider, G. and Strobach, K.: The September 3, 1978, Swabian Jura Earthquake. *Tectonophysics*, 68 (1-2), 1-14, 1980.

Heidbach, O., Rajabi, M., Reiter, K., and Ziegler, M., WSM Team: World Stress Map Database Release 2016. V. 1.1. GFZ Data Services. <http://doi.org/10.5880/WSM.2016.001>, 2016.

775 Hetényi G., Molinari I., Clinton J., Bokelmann G., Bondár I., Crawford W. C., Dessa J.-X., Doubre C., Friederich W., Fuchs F., Giardini D., Gráczér Z., Handy M. R., Herak M., Jia Y., Kissling E., Kopp H., Korn M., Margheriti L., Meier T., Mucciarelli M., Paul A., Pesaresi D., Piromallo C., Plenefisch T., Plomerová J., Ritter J., Rümpker G., Šipka V., Spallarossa D., Thomas C., Tilmann F., Wassermann J., Weber M., Wéber Z., Wesztergom V., Živčić M., AlpArray Seismic Network Team, AlpArray OBS Cruise Crew, AlpArray Working Group: The AlpArray Seismic Network: a large-scale European experiment to image the Alpine orogen. *Surveys in Geophysics* (2018) (Open Access), 1-25, <https://doi.org/10.1007/s10712-018-9472-4>, 2018.

780

Hiller, W.: Eine Erdbebenwarte im Gebiet der Schwäbischen Alb. *Zeitschrift für Geophysik*, 9: 230-234, 1933.

785 Houlié, N., Woessner, J., Giardini, D. and Rothacher, M.: Lithosphere strain rate and stress field orientations near the Alpine arc in Switzerland. *Scientific reports*, 8(1), 1-14, 2018.

Feldfunktion geändert

Husen, S., Kissling, E., Deichmann, N., Wiemer, S., Giardini, D., and Baer, M.: Probabilistic earthquake location in complex three-dimensional velocity models: Application to Switzerland. *Journal of Geophysical Research*, 108(B2), 2077, <https://doi.org/10.1029/2002JB001778>, 2003.

Feldfunktion geändert

790

Illies, J. H.: Der Hohenzollerngraben und Intraplattenseismizität infolge Vergitterung lamellärer Scherung mit einer Riftstruktur. *Oberrhein. Geol. Abh.*, 31, 47-78, 1982.

795

Kastrup, U., Zoback, M. L., Deichmann, N., Evans, K. F., Giardini, D., and Michael, A. J.: Stress field variations in the Swiss Alps and the northern Alpine foreland derived from inversion of fault plane solutions. *Journal of Geophysical Research*, 109, B01402, 2004.

800

[Kennett, B. L. N., Engdahl, E. R., and Buland, R. \(1995\). Constraints on seismic velocities in the Earth from traveltimes. *Geophysical Journal International*, 122 \(1\), 108-124.](#)

hat formatiert: Schriftart: 10 Pt., Englisch (Vereinigte Staaten)

hat formatiert: Schriftart: 10 Pt., Nicht Fett, Englisch (Vereinigte Staaten)

hat formatiert: Schriftart: 10 Pt., Englisch (Vereinigte Staaten)

hat formatiert: Schriftart: 10 Pt.

hat formatiert: Schriftart: 10 Pt., Nicht Kursiv, Englisch (Vereinigte Staaten)

hat formatiert: Schriftart: 10 Pt., Englisch (Vereinigte Staaten)

Kissling, E., Ellsworth, W. L., Eberhart-Phillips, D., and Kradolfer, U.: Initial reference models in local earthquake tomography. *Journal of Geophysical Research: Solid Earth*, 99(B10), 19635-19646, 1994.

805

Kissling, E., Kradolfer, U. & Maurer, H.: Program VELEST user 's guide – Short Introduction. Institute of Geophysics, ETH Zürich, 1995.

Kunze, T.: Seismotektonische Bewegungen im Alpenbereich, Doktorarbeit, Universität Stuttgart, 1982.

810

Leydecker, G.: Erdbebenkatalog für Deutschland mit Randgebieten für die Jahre 800 bis 2008. *Geologisches Jahrbuch*, E 59, E. Schweizerbart'sche Verlagsbuchhandlung, Stuttgart, 2011.

Lomax, A., Virieux, J., Volant, P., and Berge-Thierry, C.: Probabilistic earthquake location in 3D and layered models: introduction to a Metropolis-Gibbs method and comparison with linear locations. In Thurber, C., Rabinowitz, N. (eds), *Advances in seismic event location*, Springer, Dordrecht, 101-134, 2000.

815

[Mader, S., Ritter, J.R.R.: The StressTransfer Seismic Network - An Experiment to Monitor Seismically Active Fault Zones in the Northern Alpine Foreland of Southwestern Germany. *Seismol. Res. Lett.*, in print doi: 10.1785/0220200357.](#)

820 Meschede, M., and Warr, L. N.: The Geology of Germany: A Process-Oriented Approach. Regional Geology Reviews, Springer Nature Switzerland AG, 2019.

[Michael, A.J., 1984. Determination of stress from slip data: Faults and folds, J. Geophys. Res. 89, 11.517-11.526.](#)

825 Müller, B., Zoback, M.L., Fuchs, K., Mastin, L., Gregersen, S., Pavoni, N., Stephansson, O. and Ljunggren, C.: Regional patterns of tectonic stress in Europe. J. Geophys. Res., 97(B8), 11783-11803, 1992.

[Onescu, M.C., Rizescu, M. & Bonjer, K.P.: SAPS—a completely automated and networked seismological acquisition and processing system. Comp. Geosci., 22, 89–97, 1996.](#)

830

[Plenefisch, T. and Bonjer, K.-P.: The stress field in the Rhine Graben area inferred from earthquake focal mechanisms and estimation of frictional parameters. Tectonophysics, 275, 71-97, 1997.](#)

Podvin, P., and Lecomte, I.: Finite difference computation of traveltimes in very contrasted velocity models: a massively parallel approach and its associated tools. Geophysical Journal International, 105(1), 271-284, 1991.

835

Regierungspräsidium Freiburg, Landesamt für Geologie, Rohstoffe und Bergbau (Hrsg.): LGRB-Kartenviewer – Layer GÜK300: Tektonik, <https://maps.lgrb-bw.de/>, last access: 28th March 2019

840 Regierungspräsidium Freiburg, Landesamt für Geologie, Rohstoffe und Bergbau: Last felt earthquakes in Baden-Württemberg, <https://lgrb-bw.de/erdbehen/erdbebenmeldung>, last access: 28th August 2020

Feldfunktion geändert

Reicherter, K., Froitzheim, N., Jarosinski, M., Badura, J., Franzke, H. J., Hansen, M., ... and Stackebrandt, W.: Alpine tectonics north of the Alps. The geology of central Europe, 2, 1233-1285, 2008.

845

Reinecker, J. and Schneider, G.: Zur Neotektonik der Zollernalb: Der Hohenzollergraben und die Albstadt-Erdbeben. Jahresberichte und Mitteilungen des Oberrheinischen Geologischen Vereins, 391-417, 2002.

850 Reinecker, J., Tingay, M., Müller, B., and Heidbach, O.: Present-day stress orientation in the Molasse Basin. Tectonophysics, 482(1-4), 129-138, 2010.

Reiter, K., Heidbach, O., Reinecker, J., Müller, B. and Röckel, T.: Spannungskarte Deutschland 2015. Erdöl Erdgas Kohle, 131, 11, 437-442, 2015.

Feldfunktion geändert

855

[Ring, U., & Bolhar, R. \(2020\). Tilting, uplift, volcanism and disintegration of the South German block. *Tectonophysics*, 795, 228611.](#)

860

Rivera, L., and Cisternas, A.: Stress tensor and fault plane solutions for a population of earthquakes. BSSA, 80(3), 600-614, 1990.

865

Rupf, I. and Nitsch, E.: Das Geologische Landesmodell von Baden-Württemberg: Datengrundlagen, technische Umsetzung und erste geologische Ergebnisse. Regierungspräsidium Freiburg – Abteilung 9, Landesamt für Geologie, Rohstoffe und Bergbau, 2008.

Schädel, K.: Geologische Übersichtskarte 1:100.000 C7918 Albstadt und Erläuterungen. Geologisches Landesamt Baden-Württemberg, Freiburg i. Br., 44pp, 1976.

870

Schneider, G.: Seismizität und Seismotektonik der Schwäbischen Alb, F. Enke Verlag, Stuttgart, 1971.

Schneider, G.: Die Erdbeben in Baden-Württemberg: 1963-1972, Inst. für Geophysik der Univ. Stuttgart, 1973.

875

Schneider, G.: The earthquake in the Swabian Jura of 16 Nov. 1911 and present concepts of seismotectonics. Tectonophysics, 53, 279–288, 1979.

Schneider, G.: Das Beben vom 3. September 1978 auf der Schwäbischen Alb als Ausdruck der seismotektonischen Beweglichkeit Suedwestdeutschlands. Jahresberichte und Mitteilungen des Oberrheinischen Geologischen Vereins, N. F., 62, 143–166, 1980.

880

Schneider, G.: Beziehungen zwischen Erdbeben und Strukturen der Süddeutschen Großscholle, Neues Jahrbuch für Geologie und Palaäntologie – Abhandlungen, 189, 275–288, 1993.

885

Sieberg, A. and Lais, R.: Das mitteleuropäische Erdbeben vom 16.11.1911, Bearbeitung der makroseismischen Beobachtungen. Veröffentlichungen der Reichsanstalt für Erdbebenforschung Jena, H. 4, Jena, 1925.

Snoke, J. A.: FOCMEC: Focal mechanism determinations. *International Handbook of Earthquake and Engineering Seismology*, 85, 1629-1630, 2003.

890 Stange, S. and Brüstle, W.: The Albstadt/Swabian Jura seismic source zone reviewed through the study of the earthquake of March 22, 2003. *Jahresberichte und Mitteilungen des Oberrheinischen Geologischen Vereins*, 391-414, 2005.

Stange, S.: Erdbebenüberwachung Baden-Württemberg – Das modernisierte Starkbeben- und Detektionsmessnetz. LGRB – Nachricht, Regierungspräsidium Freiburg, Nr. 2018/07, 2018.

895 Tarantola, A. and Valette, B.: Inverse problems = quest for information, *J. Geophys.*, 50, 159-170, 1982.

Turnovsky, J.: Herdmechanismen und Herdparameter der Erdbebenserie 1978 auf der Schwäbischen Alb. Doktorarbeit, Universität Stuttgart, 1981.

900 Tyagunov, S., Grünthal, G., Wahlström, R., Stempniewski, L., and Zschau, J.: Seismic risk mapping for Germany. *Nat. Hazards Earth Syst. Sci.*, 6, 573-586, 2006.

[Valley, B., Evans, K.F.: Stress state at Soultz to 5 km depth from wellbore failure and hydraulic observations. Proceedings, Thirty-Second Workshop on Geothermal Reservoir Engineering, Stanford University, Stanford, California, 2007.](#)

905

[Vavryčuk, V., 2014. Iterative joint inversion for stress and fault orientations from focal mechanisms, *Geophysical Journal International*, 199, 69-77, doi: 10.1093/gji/ggu224.](#)

910 Wessel, P., Luis, J. F., Uieda, L., Scharroo, R., Wobbe, F., Smith, W. H. F., and Tian, D: The Generic Mapping Tools version 6. *Geochemistry, Geophysics, Geosystems*, 20, 5556–5564. <https://doi.org/10.1029/2019GC008515>, 2019.

Wetzel, H.-U. and Franzke, H. J.: Lassen sich über die Fernerkundung erweiterte Kenntnisse zur seismogenen Zone Bodensee-Stuttgart (9°-Ost) gewinnen? *Publikationen der Deutschen Gesellschaft für Photogrammetrie und Fernerkundung*, 12, 339–347, 2003.

915

Xu, Z., Wang, S., Huang, Y., and Gao, A.: Tectonic stress field of China inferred from a large number of small earthquakes. *Journal of Geophysical Research: Solid Earth*, 97(B8), 11867-11877, 1992.

hat formatiert: Englisch (Vereinigte Staaten)

Feldfunktion geändert

Zoback, M. L.: First-and second-order patterns of stress in the lithosphere: The World Stress Map Project. *Journal of Geophysical Research: Solid Earth*, 97(B8), 11703-11728, 1992.

925